A 3-D Model for the Operation of a Radiation Pyrometer in an Axial Flow Turbine

by

David A. Williams

Thesis submitted to the Faculty of the

Virginia Polytechnic Institute and State University

in partial fulfillment of the requirements for the degree of

Master of Science

in

Mechanical Engineering

APPROVED:

Dr. Walter F. O'Brien, Chairman	Dr. H. L. Moses
Dr. A. Myklebust	Dr. B. Vick

September, 1987

Blacksburg, Virginia

A 3-D Model for the Operation of a Radiation Pyrometer in an Axial Flow Turbine

by

David A. Williams

Dr. Walter F. O'Brien, Chairman

Mechanical Engineering

(ABSTRACT)

An accurate knowledge of turbine blade surface temperature is desired in order to obtain maximum performance from turbine engines. A limited spectrum radiation pyrometer can be used for blade temperature measurement. A model is presented which predicts the output signal from the detector unit of a pyrometer in a turbine engine application.

Six inputs are required for the model. The inputs are the turbine blade geometry, location of the pyrometer with respect to the blades being viewed, focusing parameters of the pyrometer, type of detector, transmission curve of the optical system, and an estimate of the blade surface temperature. The model uses Fortran 77 and IBM CADAM to create a three dimensional representation of the pyrometer path across the blades along with the intercepted target spots. Once the target spot areas are determined, the photocurrent output signal of the detector is predicted as a function of percent blade chord and time. Results are shown for different detectors and temperature distributions. Experimental data is also included, and a comparison is made between the data and the model.

Any of the model input parameters can be varied so that different pyrometer schemes can be evaluated at either the initial design phase or after installation.

Acknowledgements

I would like to thank Gerry Micklow for his guidance and also his encouragement to attend graduate school. Dr. O'Brien was an excellent person to have as my advisor. I learned a great deal about research, gas turbines, and technical writing while working with him. I would like to thank Dr. O'Brien along with the people from Rosemount Aerospace Division for giving me the opportunity to work on this project. It was an excellent research project because it exposed me to several facets of engineering. Rick O'Brien provided a great deal of insight and helped with the creation of the model. I would also like to thank my other committee members, Dr. Myklebust, Dr. Moses, and Dr. Vick, for being on my committee and making it possible for me to complete this work. Dr. Myklebust was especially helpful with the CAD work in the early phases of this project. Finally, I would like to thank my wife, Marnie, for all of her patience, understanding and good cooking. I would also like to thank her for proofreading and typing this paper.

Table of Contents

List of Illustrations

List of Tables

Nomenclature

XLOC	x coordinate for blade cross section geometry
YLOC	y coordinate for blade cross section geometry
ZLOC	z coordinate for blade cross section geometry
α	stagger angle of blade cross section
XDIST	x coordinate for lens location
YDIST	y coordinate for lens location
ZDIST	z coordinate for lens location
φ	angle between line of sight and x-y plane
θ	angle between line of sight and x-z plane
FDIST	focal distance of lens
D	lens diameter
d	target spot diameter
s	lens sighting distance to target spot
F	optical throughput
w	viewable blade width
H	percent blade height

X/C	percent blade chord
N2	engine speed
I	photocurrent
T	target temperature
Ω	solid angle
A	target area
ΩA	optical invariant
R	detector responsivity
η	optical transmission factor
λ	wavelength
L	blackbody radiation
C_1	radiation constant
C_2	radiation constant
TIME	blade passing time
BPT	blade passing time between target spots
CMIN	minimum percent chord value of viewable blade width
CMAX	maximum percent chord value of viewable blade width
f	frequency

Subscripts

s	system
f	focused target spot
b	blade

Chapter 1

Background

1.1 Introduction

The intent of this portion of the thesis is to give the reader an understanding of the importance of radiation pyrometry in turbine engines and also to describe some fundamental operating characteristics. A discussion of the pyrometer program by the Center for Turbomachinery and Propulsion Research at Virginia Tech is also given. Finally, the importance of the present work in support of this program is described. The following information concerning temperature measurement and operating characteristics of a pyrometer system came from various papers, and the references are included in the literature review.

Gas turbine engine manufacturers desire a high turbine inlet temperature in order to obtain maximum performance and high thermal efficiencies from the engine. Turbine

inlet temperature is limited by blade material. Excessive thermal loading of turbine blades can lead to shorter engine life and turbine disk failure. Two current areas of research which are aimed at obtaining the highest possible turbine inlet temperature are blade cooling designs and the development of an accurate method to measure turbine blade temperature. This research work involves measuring blade temperature through the use of a limited spectrum radiation pyrometer.

1.2 Blade Temperature Measurement Techniques

There are several methods available today for measuring blade temperature. One is the use of an ITT (intermediate turbine temperature) gage. A typical ITT gage works by using an analog thermocouple circuit which takes measurements at the engine inlet and exit. A relationship is determined between the two measurements which is a function of the engine bypass ratio. The result is an estimate of the gas temperature in the turbine. The accuracy of this measurement is approximately plus or minus 86 degrees C [1]. Thermal paints are another possible measurement technique. These paints change color at a specific temperature. However, available temperature increments for these paints is limited, only maximum blade temperature can be determined, and inspection of the paint can be done only after engine runs. So thermal paints do not lend themselves to applications for real time measurements of blade temperature. Imbedding thermocouples in turbine blades is another possible alternative but has several shortcomings. Thermocouples tend to weaken the mechanical strength of the blade and also have a poor response time. It is also difficult to transmit a thermocouple signal from the turbine wheel which is rotating at very high speeds.

With accuracies as high as plus or minus 15 degrees C, a fast response time, and a non-contacting nature, the radiation pyrometer is probably the best method for measuring blade surface temperature. Pyrometers can be used to obtain an average blade temperature for control purposes, to determine a detailed thermal map or profile of the blade for research and diagnostics, and to detect hot blades which could be the result of blocked cooling passages.

Engine pyrometry encompasses several aspects of engineering. These are materials technology, electronic engineering, signal processing, fluid mechanics, and heat transfer. The basic components of a pyrometer system are shown in Figure 1. The probe contains a lens system which focuses the emitted radiation of a target spot on a turbine blade onto a photovoltaic detector via fiber optics. Next, the output current of the detector is passed through an amplifier. The voltage output of the amplifier is transmitted through signal processing and then digitized on a high speed analog to digital converter (A/D) and the results are recorded on a computer. The calibration of the pyrometer will determine the relationship between voltage and temperature.

Photovoltaic detectors are very temperature sensitive and the use of fiber optics allows the detector to be removed from the hot section of the engine. The detector receives radiation from a limited portion of the light spectrum and produces a photocurrent. The range of wavelengths in which the detector receives radiation and the amplitude of the photocurrent is dependent upon the type of detector being used. Silicon (Si) detectors are less sensitive to thermal drift than other detectors, and therefore are the most widely used detectors in pyrometer work. Si detectors operate in the wavelength range of 0.2 to 1.3 microns. However, at lower blade temperatures, Si detectors produce a very low photocurrent, and this makes the signal more susceptible to noise. Indium Gallium

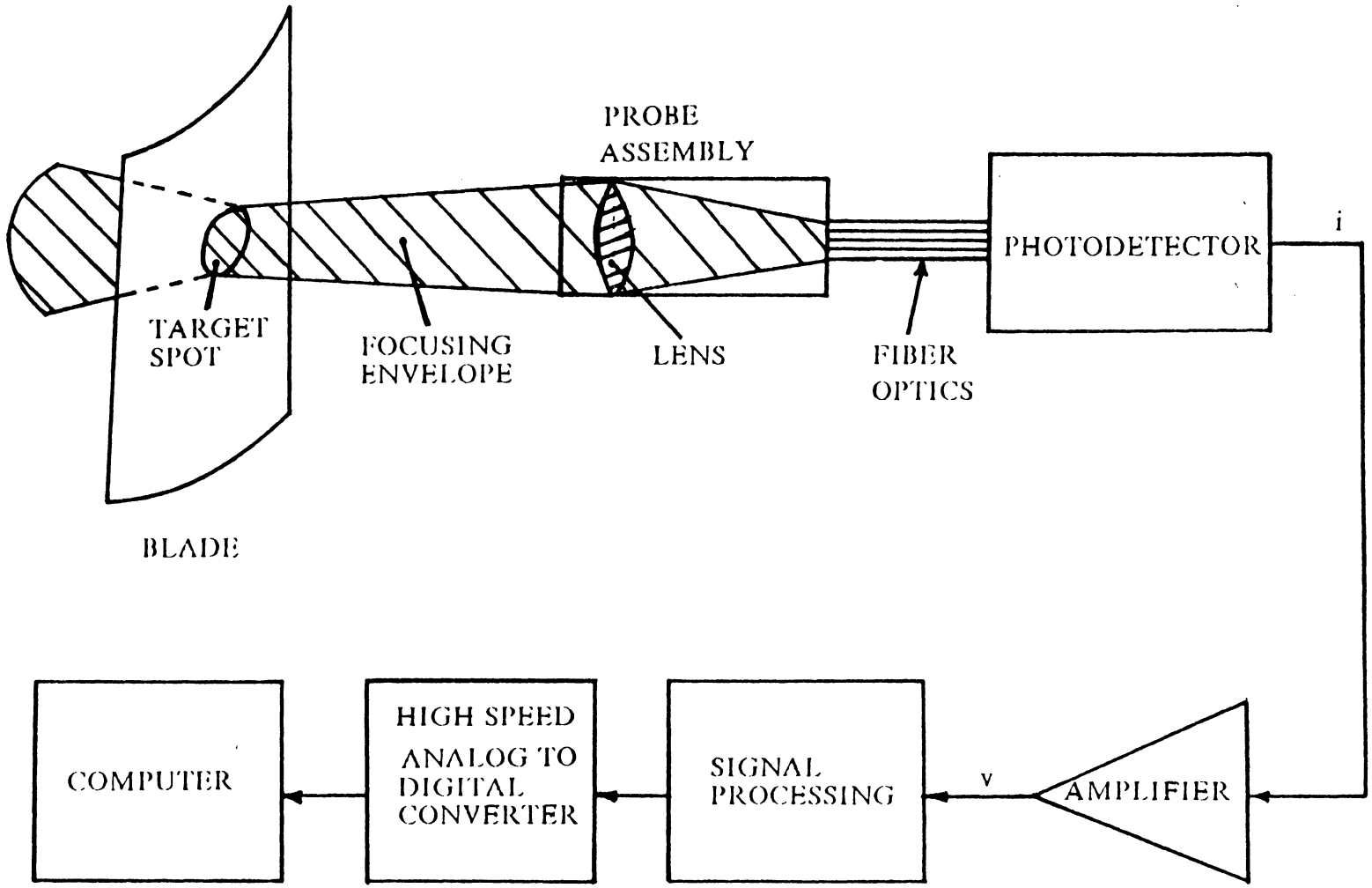

Figure 1. Schematic of a Pyrometer System

Arsenide (In Ga As) detectors have a higher output current than Si detectors but are more sensitive to surrounding temperature changes. In Ga As detectors operate in the wavelength range between 0.5 and 1.75 microns.

Any contamination that attaches to the lens system of a pyrometer will cause the pyrometer to return an improper signal. Therefore the lens must be kept clean. Two methods for lens cleaning are the use of the coanda effect with purge air and the use of a hot lens. The coanda effect is the fluid dynamic attachment of purge air to the lens which prevents any particulate contamination. The purge air is usually supplied by the compressor. The schematic of a typical purge air design is shown in Figure 2. If the lens is located in an environment where the temperature is approximately 725 degrees C, then any hydrocarbons will be burned off.

Determining the overall accuracy of a pyrometer system is very difficult because of the many uncertain variables. One major problem is the radiation received by the pyrometer which is due to reflections and not blade emission. Reflection sources include neighboring blades, static vanes, combustor walls, and flames. Flames are the most serious problem. Spurious radiation from flames can produce maximum errors of 50 to 100 degrees C. This source of error can be greatly reduced if only the suction side of the blade is viewed. If the pressure side is viewed, then a dual spectrum pyrometer is used to remove the reflection effects. A dual spectrum pyrometer has two channels. Each channel operates over a different range of wavelength. The radiant energy received from the two different spectra can be used to eliminate the reflected radiation from the signal.

Other sources of error are due to the optics and electronics. Studies have shown that "out of focus" target spots contribute minimal error [2]. Radiant energy can be lost while being transmitted through the fiber optics to the detector. The effectiveness of a

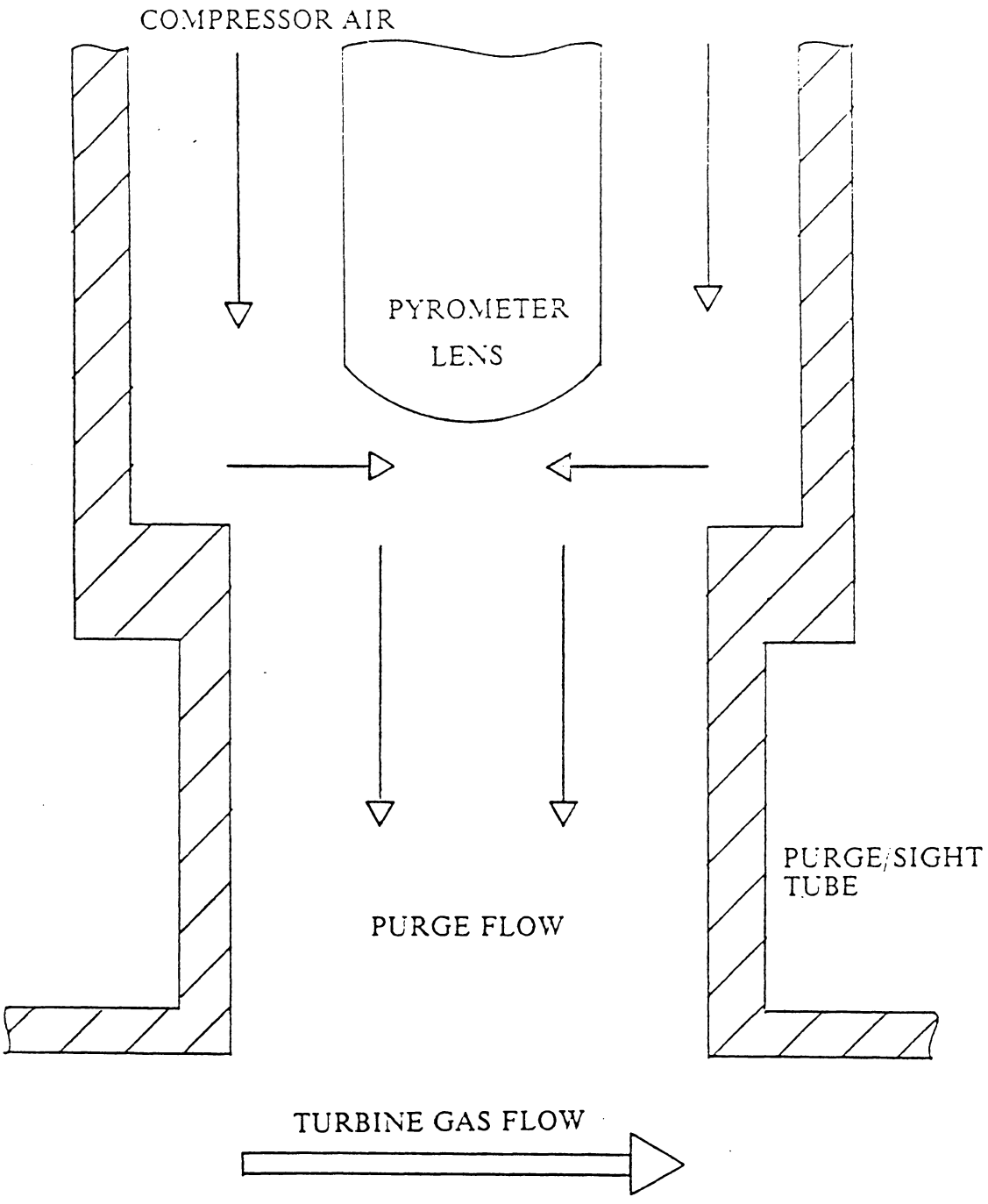

Figure 2. Sectional Schematic of Pyrometer Purge Employing Coanda Effect

fiber optic system is characterized by a transmission curve. The optical transmission curve is a function of wavelength. An optical transmission factor equal to one would imply that one hundred percent of the radiation received by the pyrometer lens system reached the detector. Research is currently being done to identify the best fiber optic design. If the A/D conversion can be considered to have small error, then the next source of error is in the detector/amplifier unit. Therefore, to obtain good accuracy with a pyrometer, a maximum signal-to-noise ratio, a fast response time, and small distortions are the objectives of a detector/amplifier design.

1.3 Research Program

The present research work is part of a pyrometer research program supported by Rosemount Aerospace Division. A test cell containing a Pratt and Whitney JT15D-1 turbofan engine is located at the Virginia Tech Airport. This is a twin spool engine, with approximately 2000 pounds of thrust, typically used on small business aircraft. The spool containing the high temperature turbine rotor can achieve design speeds up to 31,000 rpm. This first stage turbine rotor which is viewed by the pyrometer contains seventy-one blades [3]. A schematic of this engine can be seen in Figure 3. The engine has been modified by Pratt and Whitney to incorporate penetrations for two pyrometers. The pyrometer installation is shown in Figure 4. The data acquisition system for the pyrometers consists of a Lecroy high speed digitizer and an IBM PC-AT. The Lecroy can capture and digitize the pyrometer signal at a rate of 1 MHz. The Lecroy uses a ten bit word and has a resolution of 9.8 mV.

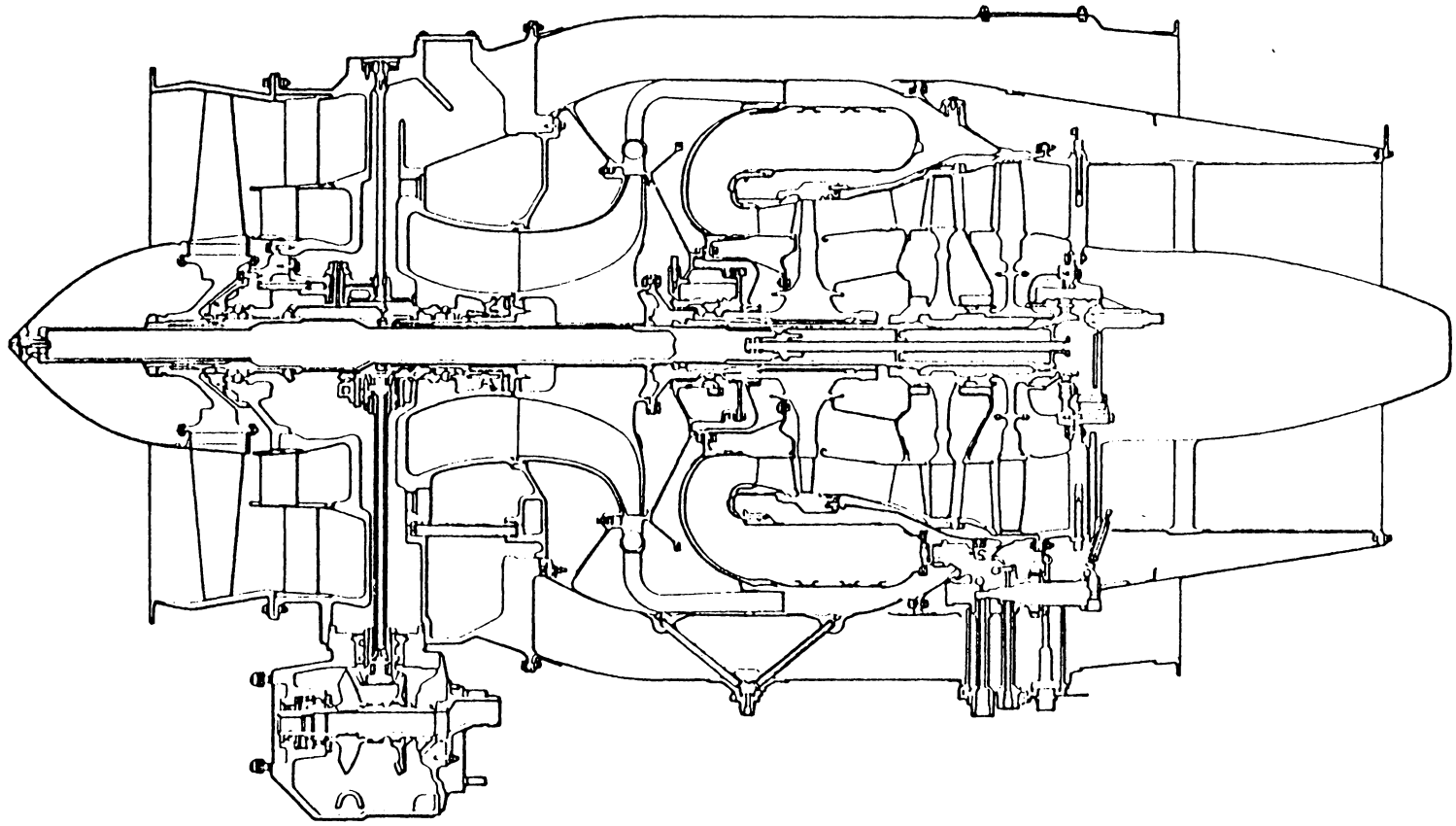

Figure 3. JT15D-1 Cross Section Schematic

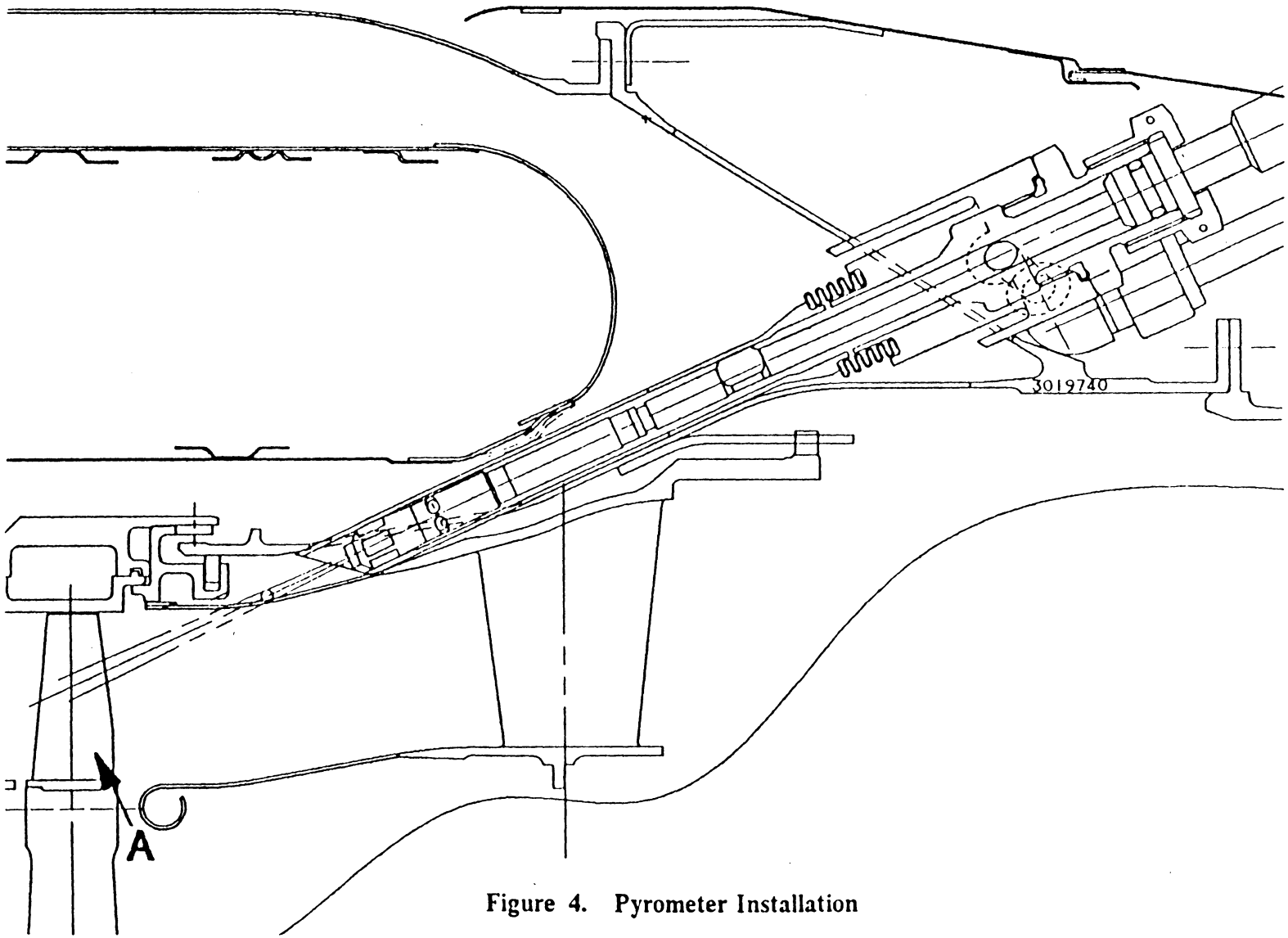

Figure 4. Pyrometer Installation

The engine is also instrumented to record percent engine speed of both spools, ITT, exhaust gas temperature (EGT), compressor temperature, compressor pressure, oil pressure, oil temperature, fuel flow rate, ambient conditions, and flow rates of the purge air system for the pyrometers. The aforementioned data is recorded on an IBM PC and on an IBM PC-AT which are operated with a common time base. This test facility is being used by Rosemount to test various pyrometers and detectors in the JT15D-1 to determine the durability and reliability of pyrometers for in flight applications. Various purge air schemes are also being evaluated to determine which is the most appropriate.

This thesis work is in direct support of the pyrometer program. A model was created which can be used to predict the output signal of a pyrometer and corresponding detector for different pyrometer installations, blade geometries, temperature distributions, and detectors. The model can be a valuable tool for the evaluation of pyrometer systems before installation in an engine. The model creates a three dimensional representation of the path the pyrometer traces across the blade along with the associated target spots. Then with an estimate of blade temperature from thermocouples, gas path analysis, or some other method, the pyrometer output signal can be modeled for any type of detector.

Chapter 2

Literature Review

There is a significant amount of research in the area of turbine blade temperature measurement. The use of a radiation pyrometer is a popular method because of a non-contacting nature and fast response time. This literature review describes the content of ten papers which are focused on the fundamental operating characteristics and problems associated with gas turbine engine pyrometry. Some of the problems discussed in these papers are: blade viewing techniques, different lens systems, different detector characteristics, methods of cleaning the lens, cooling of the probe, the use of fiber optics, signal processing, noise and error sources, and calibration methods.

Beynon [4] presents a paper which discusses basic "ground-rules" to follow when installing and operating a radiation pyrometer in a gas turbine environment. A description is given concerning the various types of radiation the pyrometer could encounter and the errors associated with each type. The role that wavelength and temperature play in determining which type of detector to use is also mentioned. In a more recent paper,

Beynon [5] discusses blade profiling, hot blade detection, and temperature averaging as different applications of pyrometers for temperature measurement. Various methods are mentioned describing ways to access or view the turbine blade. Beynon discusses a direct sight path and also the use of mirrors. The problems and solutions associated with a harsh environment, optics fouling, proper matching of electronic bandwidth with target spot size, and varying emissivity effects are also discussed.

The performance criteria required for an acceptable detector and some advanced techniques in signal processing which help overcome the severe effects of the blade environment are given in a paper by Douglas [6]. Douglas also created a computerized radiation model and compared the model with actual pyrometer data. The effects caused by varying emissivity due to reflections can create errors when analyzing a pyrometer output signal. Atkinson and Strange [7] discuss a method in which two pyrometers with different wavelengths are used to eliminate the effect of varying emissivity. Hunter, Allemand, and Thomas [8] describe the use of a multiwavelength pyrometer and show results along with an error analysis.

Kirby, Zachary, and Rui [9] compare the differences between single and multiwavelength engine pyrometry. In one of Kirby's later papers [2] an excellent overview of the operating characteristics of a radiation pyrometer is presented. This paper expresses the need for the interchangeability of pyrometer systems in various engines, especially for military applications. Kirby describes the operation of detectors and how to obtain the photocurrent output of a pyrometer system by using blackbody radiation and the spectral responsivity curve of a particular detector. A method for determining the proper spot size for a given pyrometer system when measuring peak blade temperature is also given in this paper. The effect and amount of noise is described as a function of target

temperature. Kirby gives a brief analysis that shows that defocus effects of the lens system create little error in the spatial sensitivity of the pyrometer. Also, a description of a lens cleaning system which utilizes purge air and the coanda effect to prevent any particulate contamination is given.

An excellent description of the various components of a pyrometer system is given in a paper by Koschel, Salden, and Hoch [10]. The system description includes probe head design, cooling, detector/amplifier unit and signal processing. This paper also describes an automated calibration system and the results of the calibration. In a much earlier paper, Mossey [11] presents a simpler calibration scheme along with some test results and an error analysis. More recent experimental results along with contour temperature maps of turbine blades are contained in a paper by Schulenberg and Bals [12]. Most of the previously mentioned papers describe the application of fiber optics to engine pyrometry. The recent developments in fiber optic technology have allowed the temperature sensitive detector to be placed in a location away from the hot section of the engine.

Much of the information contained in this literature review is not directly related to the present work. However, a fundamental understanding of the operating characteristics of a pyrometer system was essential in order to create a useful and realistic model that can predict a pyrometer signal. The papers mentioned in this review are very informative and are suggested to the reader for more detailed research in the area of engine pyrometry.

Chapter 3

Introduction

This thesis presents a procedure to predict the output photocurrent signal from the detector of a pyrometer system. The predicted signal is based on the emitted blackbody radiation from a target spot and does not take into account noise sources or signal processing. The creation of the modeled signal is done in two steps. First, a three dimensional wireframe model of the blade geometry, pyrometer focusing envelope and associated target spots is made by using IBM CADAM. The area of each target spot is determined from this geometric model. The second step consists of putting together the solid angle of the focusing envelope of the pyrometer, the blackbody radiation of the target spots, the spectral responsivity of the detector, the optical transmission curve, and the target spot areas. The result is the predicted photocurrent of a pyrometer detector. The details of this procedure will be discussed later in this paper.

There are six independent parameters which are input to the model. The first three sets of parameters are used to create the geometric model. The first of these is the blade

geometry. Knowledge of the blade shape at various cross sections can be obtained from an engine manufacturer. Next, the installation parameters of the pyrometer probe must be known. The installation parameters of the pyrometer consist of the distances and angles of the pyrometer lens with respect to the blade being viewed. The third set of variables for the geometric model are the focusing characteristics of the pyrometer lens system. The objective lens diameter, focused target spot diameter, and focal length of the pyrometer are the three focusing parameters which need to be known. These can be be obtained from a pyrometer manufacturer.

The fourth input is a thermal map of the temperature distribution of the blade. This thesis uses temperatures that were obtained from a gas path analysis done for the JT15D-1 engine for various engine speeds by MacKay [13]. Mackay's gas path analysis predicts the blade surface temperature at any location on the blade. An equation for the track of the pyrometer is determined from the geometric model and is input into the gas path analysis. The result is the blade surface temperature distribution along the path traced by the pyrometer. This temperature distribution is used to obtain the blackbody radiation from the target spots.

The responsivity curve of the detector being used and the optical transmission curve are the final inputs to the model. The detector responsivity (A/W) and optical transmission (percent) are a function of wavelength (microns). The detector responsivity and optical transmission are used in conjunction with the blackbody radiation from the target spots to determine the output level of the pyrometer detector. The responsivity curve for a detector and the transmission curve of the optical system can be obtained by a pyrometer manufacturer. Any of the six input parameters can be varied in order to evaluate different schemes for a pyrometer system.

The model is created using the aforementioned parameters along with Fortran 77, IBM CADAM Geometry Interface Module (GIM), interactive CADAM, and blackbody radiation theory. First, a code in Fortran 77 is compiled and linked with the GIM. The resulting module is executed. The resulting output is written to a CADAM DRAWFILE. The user then calls up the geometry on the terminal and follows an interactive procedure using CADAM to obtain the target spots and target spot areas. Next, a Fortran 77 code is run which utilizes blackbody radiation theory to predict the pyrometer signal. The signal, blade frequency, and target spots can then be analyzed to determine the optical throughput of the pyrometer, required response time of the detector, and required response time of the data acquisition system.

Several benefits can be obtained by use of this model. The model can be very helpful in the initial design phases. The pyrometer installation parameters can be varied to see which set locates the target spots on the most advantageous place on the blade, and to see the exact path the pyrometer will trace across the blade.

The hottest part of an uncooled turbine blade is at the leading edge and the tip. It is sometimes difficult to view the leading edge of a turbine blade due to complicated engine geometry, so a pyrometer trace that extends from root to tip would give a better temperature distribution than one that traced across the blade at one cross section. This model allows the user the freedom to try any installation to determine which is best.

The optical engineer can also try various focusing schemes. If an average temperature is desired, a large target spot is all that is needed. But if profile work is to be done, a much smaller target spot is required. The smaller target spot emits less radiation, thus producing a lower optical throughput. Optical throughput, F, describes the amount of radiation received by the detector. A high optical throughput implies a strong signal.

Strong signals are less susceptible to noise sources than weaker ones. Optical throughput is defined as follows [4]:

$$F = \frac{D^2 d^2}{s^2} \tag{3.1}$$

Equation 3.1 implies that large target spots and short distances between the target and lens lead to strong optical throughputs. So, moving the pyrometer lens closer to the target spot increases the optical throughput. Therefore, focusing parameters can be varied in conjunction with installation parameters in order to determine a pyrometer system design which produces an acceptable optical throughput. An acceptable value for optical throughput is dependent upon the type of detector being used and the anticipated target spot temperature. Acceptable values for optical throughput are usually determined according to a criteria for a minimum signal to noise ratio.

Some turbine blades may not operate at temperatures sufficiently high enough for silicon detectors. Silicon detectors are advantageous because they are not as sensitive to ambient temperature changes as other detectors, but they require higher engine temperatures to output strong signals. Various engine speeds or temperature distributions can be checked against different detectors to see which combination is the most appropriate. All or one of the parameters can be varied at a time to evaluate proposed pyrometer design schemes. After analysis of the model, the engineer can determine whether or not the installation of a pyrometer in a given engine is feasible and if good results can be achieved.

This model can also be used after a pyrometer system has been implemented to compare the predicted signal with the measured signal. This will aid in diagnosing any problems associated with signal processing and help to eliminate noise sources.

Chapter 4

Geometric Model

4.1 Introduction

A three-dimensional wireframe model of a turbine blade, pyrometer focusing envelope, and target spots for a given pyrometer installation is developed by first using Fortran 77 along with the CADAM GIM (Geometry Interface Module) and then applying interactive CADAM. To use interactive CADAM, the user must be familiar with CADAM or another similar computer aided design (CAD) system. The CADAM manuals are referenced and any unfamiliar terminology may be found in these manuals [14, 15, 16, 17]. It is suggested that the introduction to reference 14 be read before applying the model. It should be noted that the major action commands or function keys associated with interactive CADAM are denoted by capital italic letters in this thesis. The inputs required for the geometric model are the blade geometry at various cross sections, the radial distance from the engine centerline to each cross section, the number

of blades on the turbine disk, and the installation and focusing parameters of the pyrometer. The pyrometer installation and focusing parameters determine the orientation of the focusing envelope.

4.2 Geometry Interface Module

4.2.1 Blade Geometry

The parameters needed to describe the blade geometry are the blade chord length, stagger angle, and the x and y coordinates of various points at a particular blade cross section. Figure 5 shows a representation of the blade cross sectional geometry. Each cross section is located a specific distance from the engine centerline. This distance is along the z axis. For the given blade geometry on the JT15D-1, the x and y coordinates for four cross sections at a zero degree stagger angle are known. Therefore, the code transforms each x and y point to the proper stagger angle for each different cross section. Available information for the four cross sections is at 6.0, 27.8, 49.5, and 92.1 percent blade height. Thirty-four points are known at each cross section along with the chord length and stagger angle of the cross section. The chord lengths and stagger angles are given in Table 1.

Since, for the JT15D-1 application, the pyrometer views the suction side of the blades, only the suction surface is represented in order to simplify the wireframe model. The

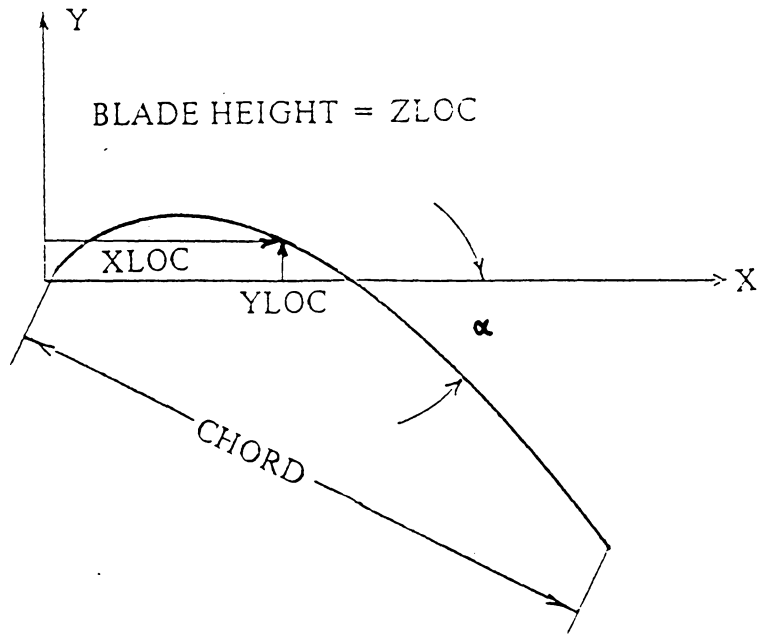

BLADE CROSS SECTION

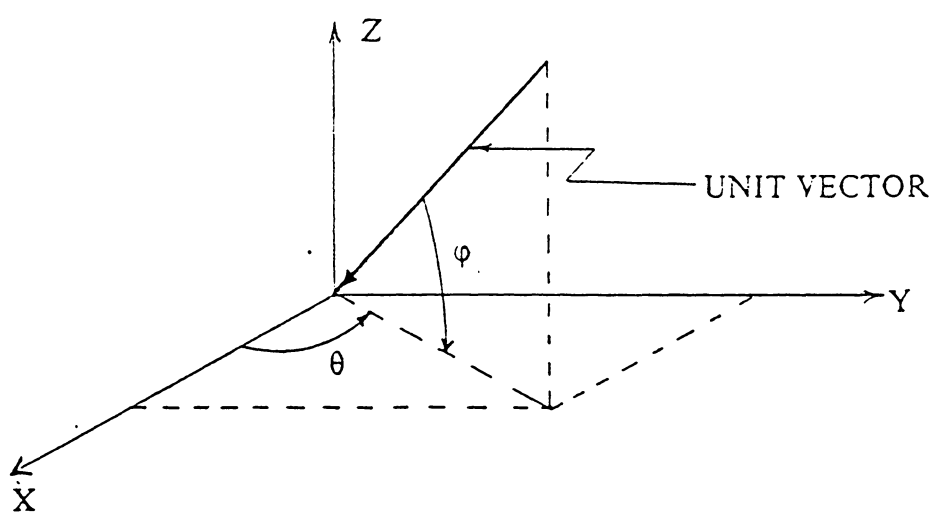

UNIT NORMALS FOR LINE OF SIGHT

Figure 5. Blade Cross Section and Unit Normals for Line of Sight

Table 1. Blade Geometry

Section	Percent Height	Chord Length	Stagger Angle
		inches	degrees
A-A	6.0	0.6611	24.42
B-B	27.8	0.6982	32.0
C-C	49.5	0.7236	38.29
D-D	92.1	0.7246	49.11

origin of the entire model is located at the leading edge of the cross section nearest to the hub. All other geometry is referenced to this origin. The CADAM GIM creates, under program control, a cubic spline between each known point of a blade cross section. Next, a ruled surface is created between each splined cross section and the result is the modeled suction surface of a turbine blade. It should be noted that for the most accurate representation of a blade, the information for an infinite number of cross sections is needed to obtain the true blade surface. However, for the present application, the blades being viewed are small and information for four cross sections is sufficient.

4.2.2 Focusing Envelope Geometry

The pyrometer installation and focusing variables describe the orientation of the focusing envelope. The pyrometer installation variables for the model are the location parameters of the objective lens with respect to the origin. The origin is located at the leading edge of the blade. The x, y, and z distances from the origin to the center of the lens, the angle between the line of sight of the pyrometer and the x-y plane (φ), and the angle between the line of sight of the pyrometer and the x-z plane (θ) describe the orientation of the pyrometer probe in the engine. This geometry is shown in Figure 6. The line of sight is defined as the centerline of the focusing envelope which passes through the center of the objective lens and the focused target spot. A representation of the normals for the line of sight is shown in Figure 5. So the unit normals for each principal axis can be described by the following equations:

$$XAXIS = \cos\varphi \cos\theta \tag{4.1}$$

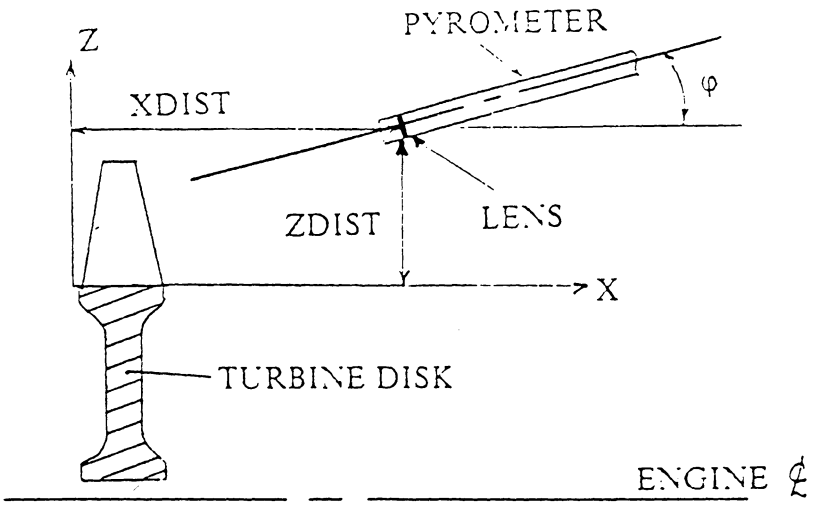

ENGINE SIDE VIEW

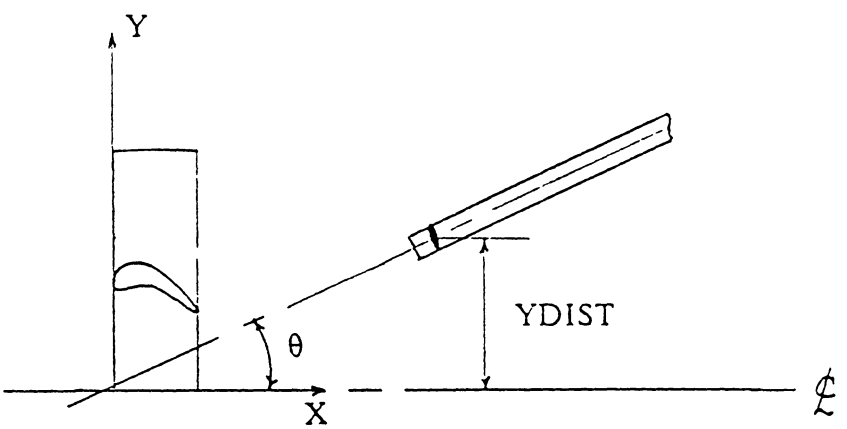

ENGINE TOP VIEW

Figure 6. Pyrometer Installation Variables

$$YAXIS = \cos\varphi \sin\theta \tag{4.2}$$

$$ZAXIS = \sin\varphi \tag{4.3}$$

Equations 4.1, 4.2, and 4.3 are necessary in order to locate the objective lens, focused target spot, and reference spot perpendicular to the line of sight of the pyrometer.

The required focusing parameters of the pyrometer are the objective lens stop diameter, focused target spot diameter, and the focusing distance of the lens. The objective lens focuses a certain distance to a focal spot. To aid the optical engineer in determining the proper distance to focus the lens, the following equation is helpful to a first approximation:

$$FDIST = \{XDIST^2 + YDIST^2 + [\tan\varphi\sqrt{XDIST^2 + YDIST^2}]^2\}^{\frac{1}{2}} \tag{4.4}$$

Where FDIST is the focal distance of the lens and the other variables are known installation parameters which have been previously defined.

A description of the focusing envelope of the pyrometer and associated variables is shown in Figure 7. The focusing envelope converges to a focal spot and then diverges again. The divergent portion of the envelope is determined by projecting dotted lines from the lens through the focal spot as shown in Figure 7. This is good to a first approximation [18]. The diameter of the reference spot can be easily calculated with a knowledge of the lens diameter, focal spot diameter, and the focal or sighting distance.

The GIM creates three circles: the lens, focal spot, and reference spot. The GIM also creates the centerline of the focusing envelope and two reference lines located inside the focal envelope parallel to and on either side of the centerline. When a cross section is

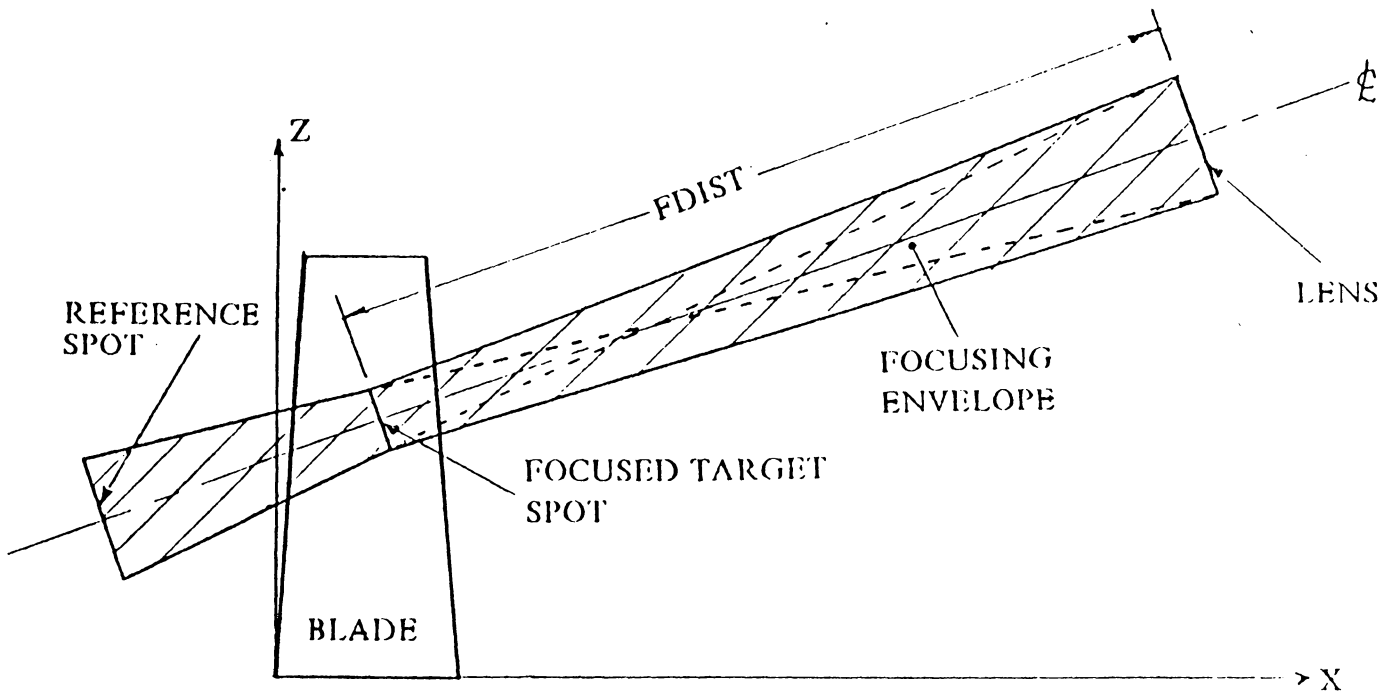

Figure 7. Focusing Envelope

removed from the focusing envelope it contains three points. These points are from the two reference lines and the centerline. The location of these points is used to map temperatures onto the target spots. The endpoints of the centerline are necessary in order to obtain an equation for the line of sight of the pyrometer. The equation for the line of sight is input into Mackay's gas path analysis to determine a temperature distribution along the portion of the blade which the pyrometer traces [13].

The resultant geometry obtained through the CADAM GIM is shown in Figure 8. This figure contains the blade suction surface geometry, objective lens, focused target spot, reference spot, centerline of focusing envelope, and reference lines. The creation of the focusing envelope and the target spots on the blade is done interactively and is described next.

4.3 Interactive Cadam

The following discussion is a simple procedure which is performed by using interactive CADAM. To fully understand this procedure, a general knowledge of CADAM is required. The reader should first note that the blade geometry and focusing envelope geometry are in two different views. The blade geometry is in the isometric view (IS) and the focusing envelope geometry is in the auxiliary view (AV). The necessity for two views will be apparent in the following paragraph.

After calling up the three dimensional drawing, the *AUX VIEW* function key is pressed and the IS view is chosen. Next, *GROUP TRAP* is used to "trap" the blade surface

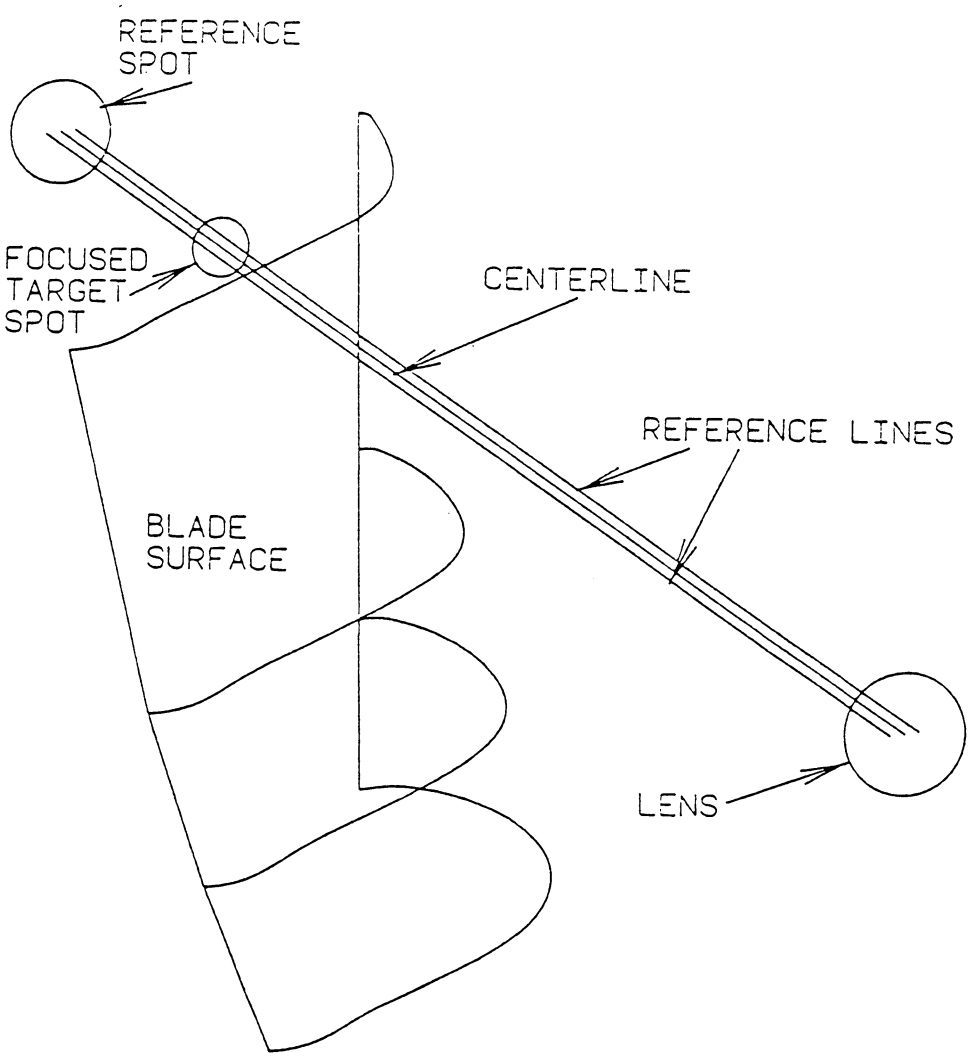

Figure 8. Resultant Geometry from GIM

geometry. *3D GROUP* and *ROT COPY STACK* are used to rotate the blade in the "group" through the proper inclination angle around the engine centerline. This creates a second bladé. The inclination angle is defined as the angle between the blades on the turbine disk. Only the blade surface geometry is included in the "group", and this is the reason for having two views. The user then follows the same procedure and rotates both blades around the engine centerline until the viewable blade width is achieved. This is shown in Figure 9. The viewable blade width, w, is the portion of the blade which the pyrometer sees.

Next the upper blade (blade 1) is erased. The lower blade (blade 2) is then rotated through the line of sight of the pyrometer. This is done by selecting *ROT COPY* and rotating blade 2 through small incremental angles around the engine centerline until the blade has traversed the inclination angle of the turbine rotor. Each blade surface created by this step represents an incremental rotation of the turbine rotor. The decision of the incremental angle is trial and error. Once the target spots are determined, this step may or may not need to be repeated. The idea is to have the target spots line up approximately tangential to one another. The target spots should not overlap very much or be very far apart from one another. If the chosen incremental angle is too small, the target spots will greatly overlap and it will be difficult to differentiate the temperature distribution between each spot. Or, if the chosen incremental angle is too large, there will be gaps between each spot and a portion of the temperature distribution will be missing from the model. So it is important to align the target spots tangential to one another. This is checked after all the target spots have been created. The movement of the blade through the line of sight of the pyrometer simulates the trace of the pyrometer path across the blade surface.

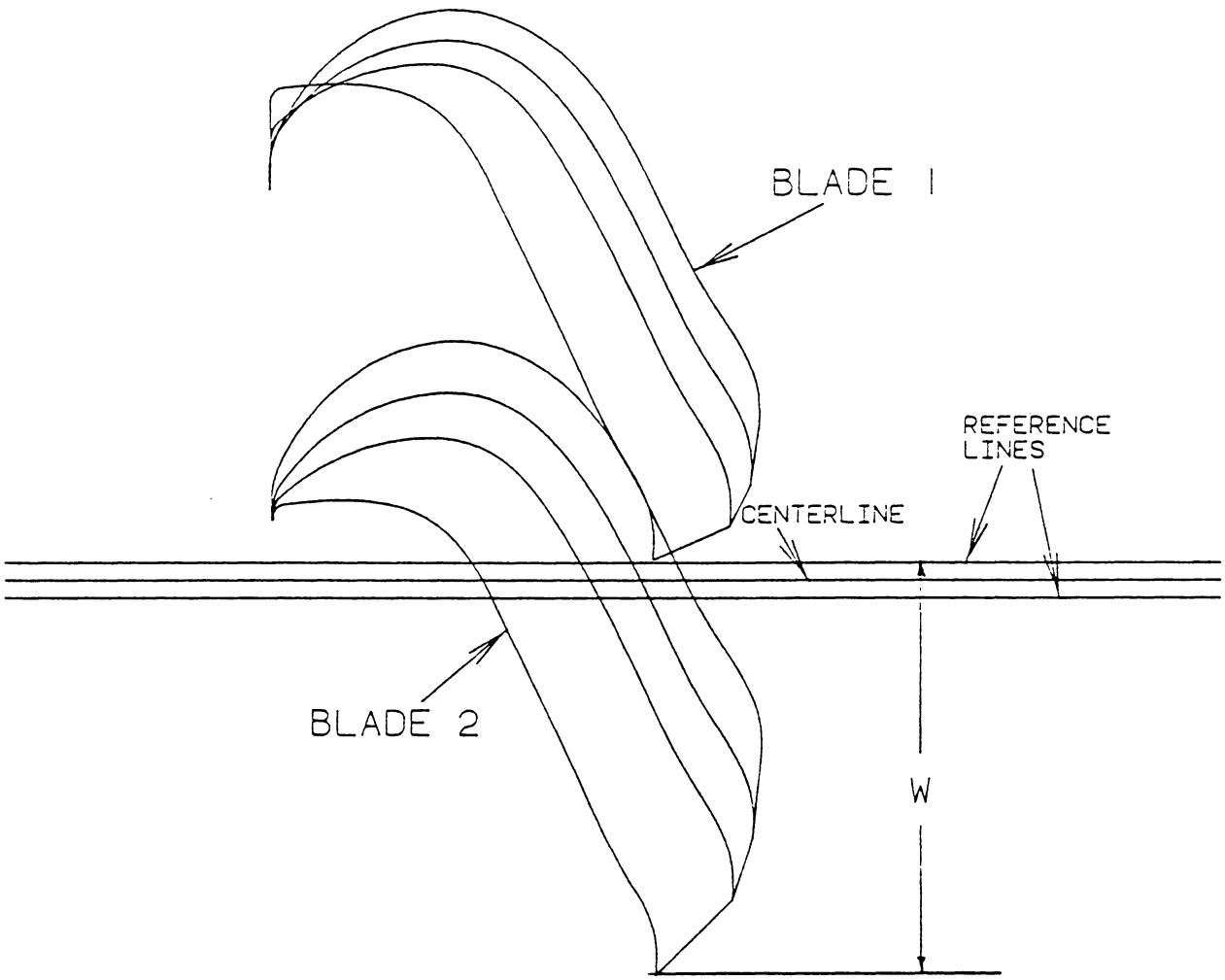

Figure 9. Viewable Blade Width

The next step is to *PROJECT* the focusing envelope geometry from the AV view to the IS view. The focusing envelope geometry consists of the lens, target spot, reference spot, reference lines, and the centerline of the focusing envelope. Once all the geometry has been projected into the IS view, ruled surfaces are created between the lens and the target spot and between the target spot and the reference spot. This creates the focusing envelope.

Using the function key *SURFACE* and *INTERSECT*, each blade surface and the surface of the focusing envelope is selected. This step creates a target spot on each blade surface. Also, using *INTERSECT*, all three lines and the blade surfaces are selected. This creates three points on each target spot which are used for temperature mapping. The resultant geometry is shown in Figure 10.

Figures 11 and 12 show two different views of three blade surfaces, the focusing envelope, and associated target spots. These figures are created by rotating three blade rows through the line of sight of the pyrometer. Figures 11 and 12 are easier to interpret than Figure 10 , but do not include the reference lines and centerline of the focusing envelope. The reference lines and centerline are required to create the points on the target spots. These points are essential for temperature mapping. Unfortunately, due to the limitations of CADAM, it is difficult to create Figures 11 and 12 with the reference lines and centerline. Therefore, these two figures are used only as a visual representation. Figure 11 shows the orientation of the path of the pyrometer and the intercepted target spots. Figure 12 is oriented so that the viewing point is at the lens of the pyrometer. This figure shows the true target spots that the pyrometer sees. If the target spots in Figure 12 do not line up approximately tangential to one another, then the former part of this procedure must be repeated with a different incremental angle.

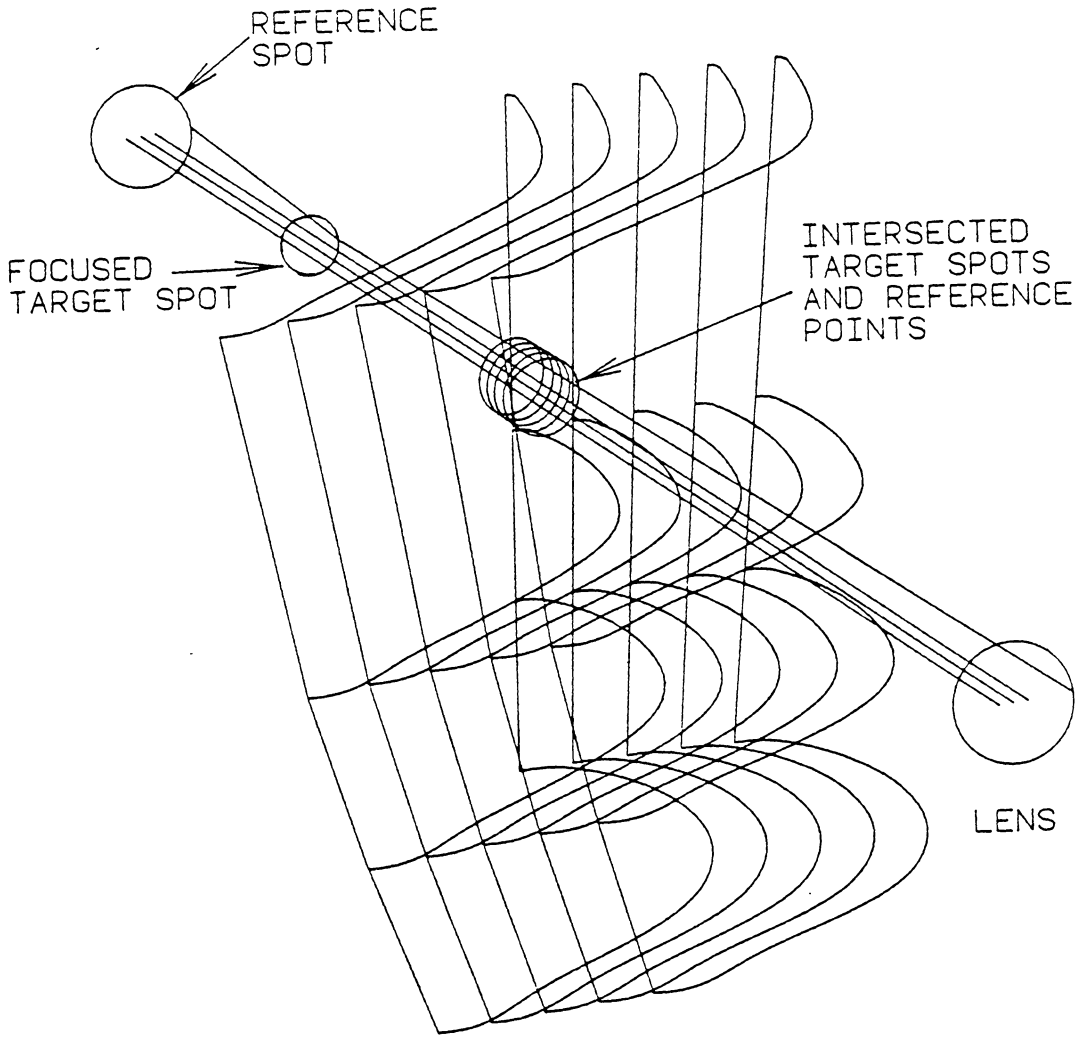

Figure 10. Resultant Geometry from Interactive Cadam

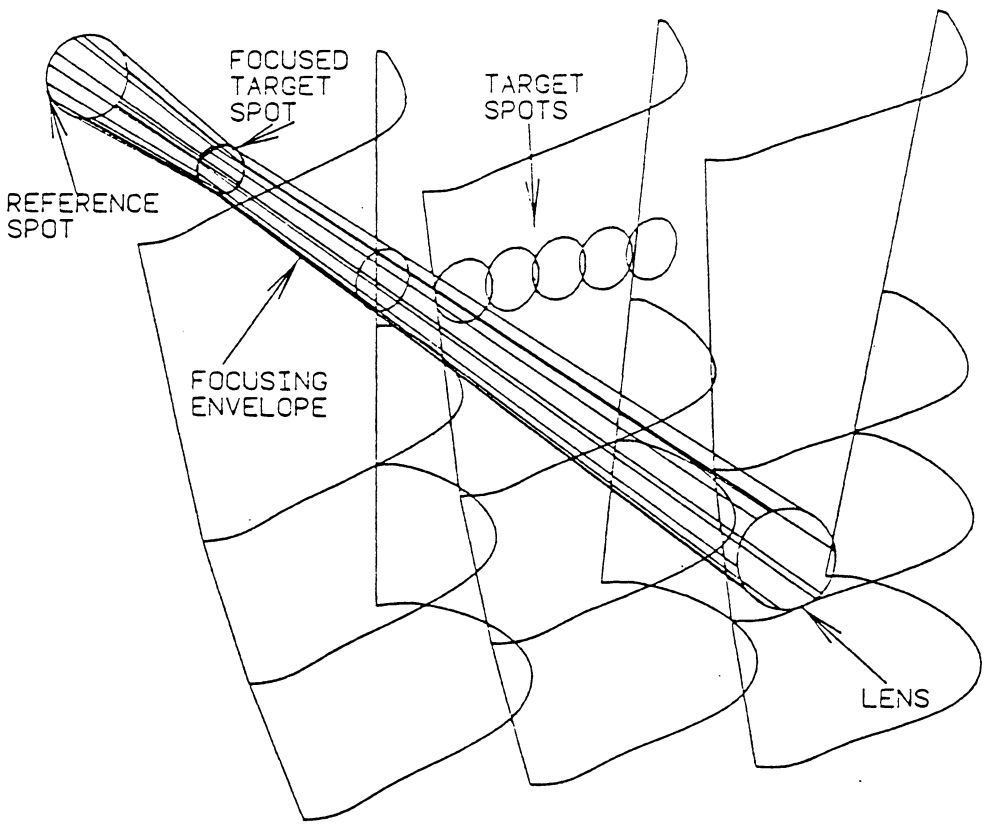

Figure 11. Trace of Pyrometer across Blades

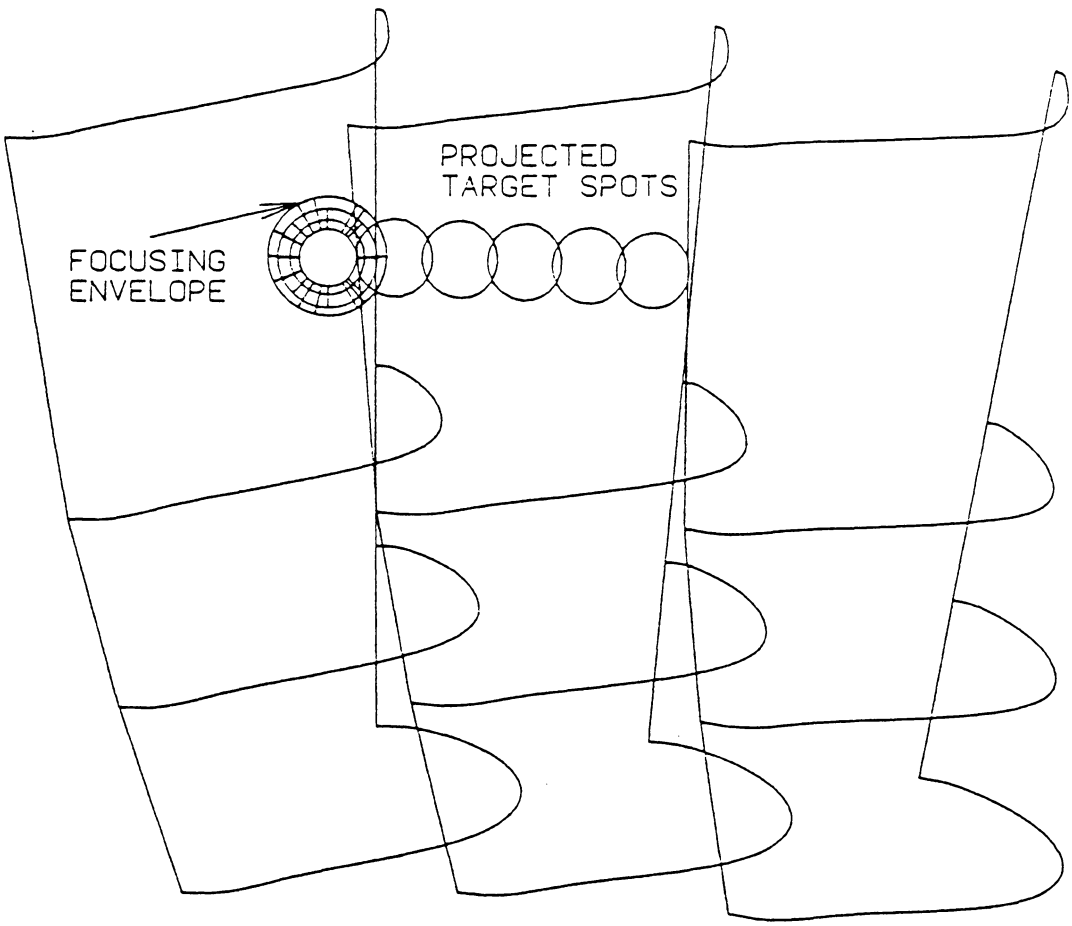

Figure 12. Target Spots

The areas in Figure 12 are the areas of the target spots on the blade surface projected normal to the focusing envelope. These projected areas are the areas required for the radiation model [19]. A representation of the projected area is shown in Figure 13.

To determine the areas of the target spots, the geometry in Figure 10 is oriented so that the viewing point is at the lens of the pyrometer. Again it should be emphasized that Figure 10 is used because it contains the points on the blade surface which are required for temperature mapping. Next, all geometry except the points and target spots are erased. Then two dimensional geometry is generated from the three dimensional geometry using the *MISC* function key. The *POINT LINE* and *SPLINE* function keys are used to divide each spot into three incremental areas as shown in figure 14. All areas and location of points on the target spots are determined by using the *ANALYSIS* function key. The location of each point on a target spot is necessary for temperature mapping which is discussed in Section 5.2.

Figure 14 shows the first target spot with incremental areas and mapped temperatures for an engine speed, N2, of ninety-five percent. N2 is the rotational speed of the gas generator of the two-spool JT15D-1. Ninety-five percent is the maximum rated speed of the gas generator, corresponding to 31120 rpm. This analysis assumes a one-dimensional approximation of the temperature gradient across a target spot. The temperature gradient found by Mackay for the JT15D-1 engine across such a small area is almost insignificant [13]. Therefore, this is considered an excellent approximation. If a cooled blade were being viewed, then a two-dimensional analysis might be required because the temperature change could be larger. The model could be modified to include reference lines that are in different planes. This would allow a two-dimensional temperature gradient to be mapped onto the target spots.

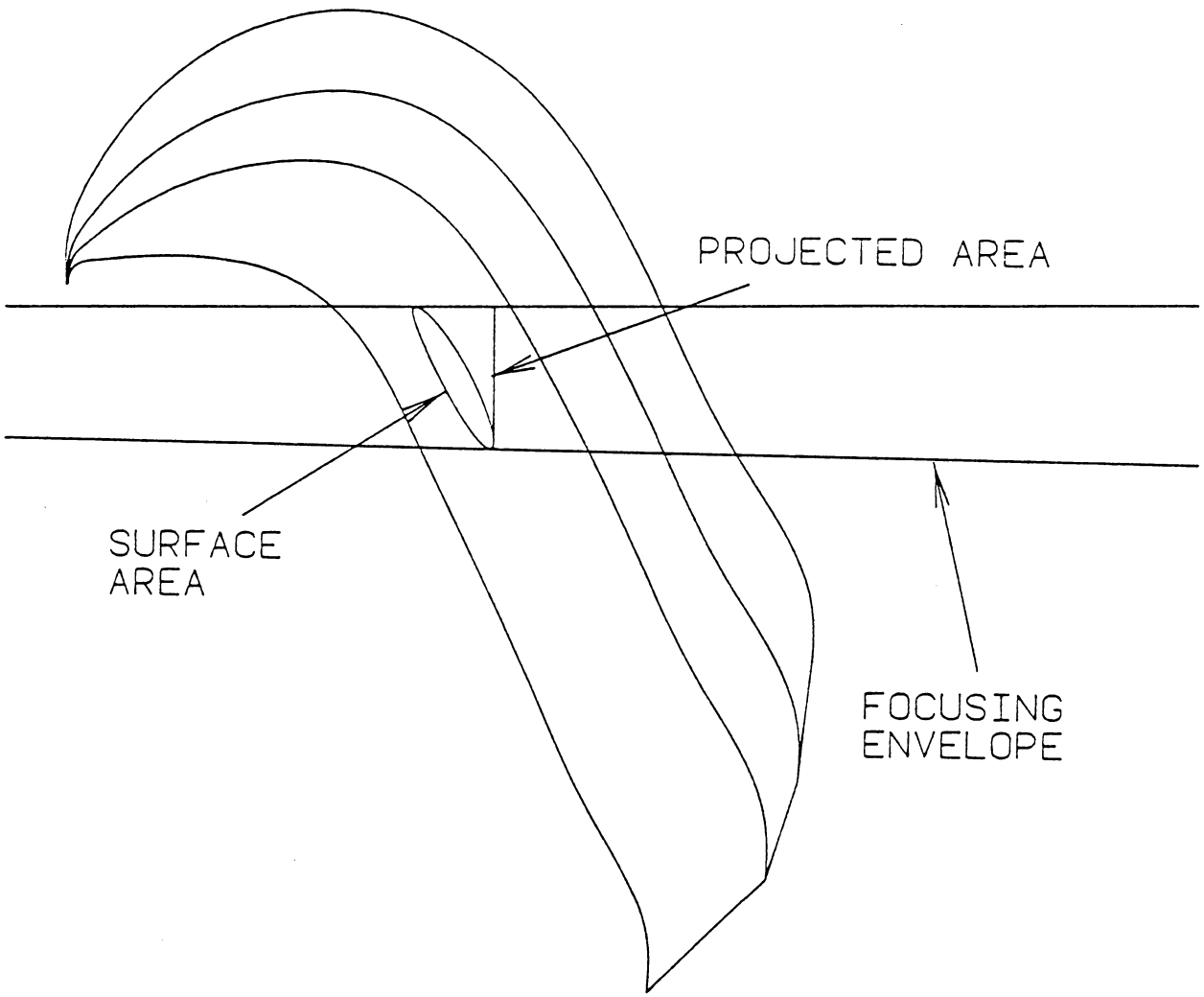

Figure 13. Projected Area

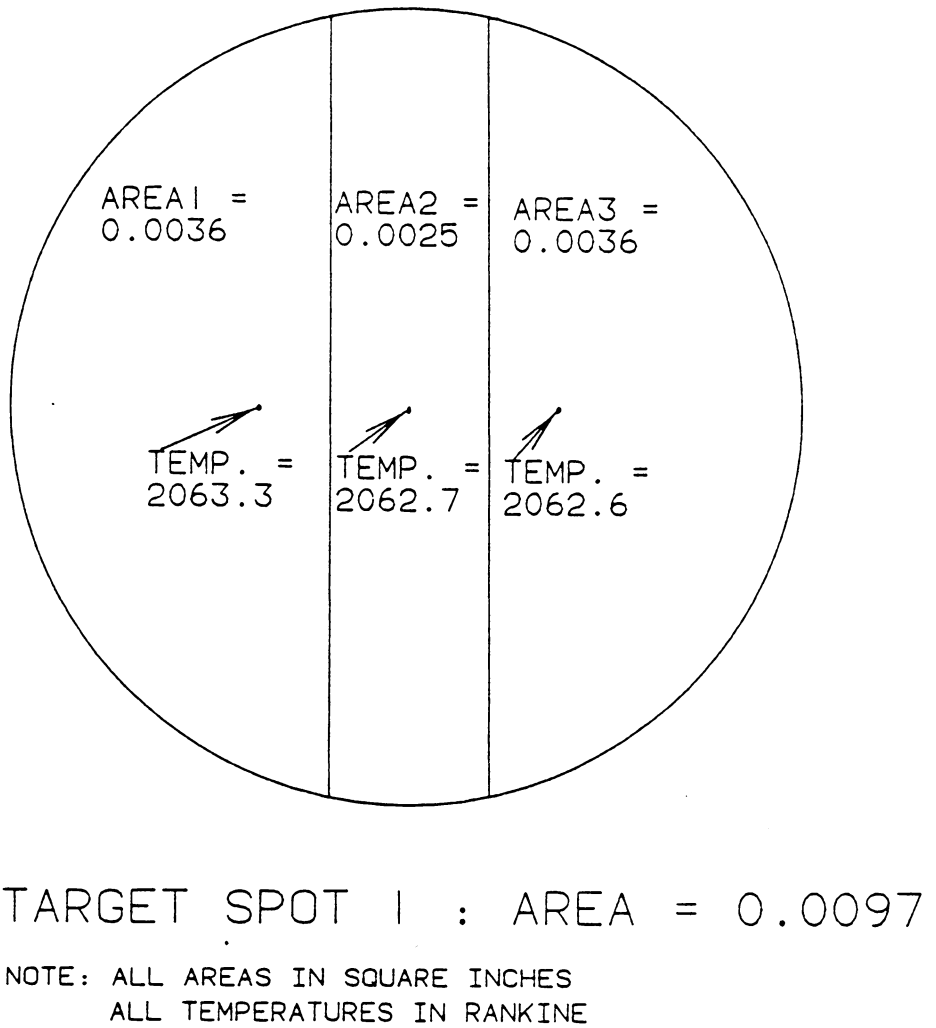

Figure 14. Temperatures from Analysis by MacKay [13]

4.4 Summary

In summary, the present geometric model can easily be created for any pyrometer application with a knowledge of the input parameters discussed at the beginning of this chapter and a basic understanding of IBM CADAM or another, similar, CAD system. The results shown in this thesis are for the blade geometry and pyrometer installation which are part of the Rosemount Research Program. The next chapter discusses the prediction of the output signal.

Chapter 5

Signal Prediction

5.1 Introduction

Five variables are required to predict the output signal of a pyrometer detector. The first set of variables is the target spot areas found from the geometric model. Next, the temperatures at each point on the target spots need to be determined. The temperature distribution is used to determine the blackbody radiation emitted from the target spots. For the JT15D-1 application, the temperature distribution is determined using a gas path analysis performed by Mackay [13]. Different engine speeds and operating conditions can be input into Mackay's work to obtain different temperature distributions. The third input parameter needed to predict a signal is the responsivity curve of the detector. The fourth input is the solid angle of radiation received by the detector from each target spot. Determining the solid angle associated with each target spot is discussed in detail later. The final variable required is the transmission curve of the optical system. The

transmission curve of a particular system is a function of wavelength. Most systems have a transmission factor which is approximately constant and slightly less than one [20].

5.2 Temperature Mapping

The radiation detected by the pyrometer is a function of the target spot temperature. The pyrometer detects an average temperature of the spot. So, several temperatures are necessary across a given target spot in order to obtain an average radiance.

The equation for the line of sight found from the geometric model is input into Mackay's gas path analysis. The result is the temperature distribution along the path of the pyrometer [13]. This temperature distribution is mapped onto the three points of each target spot. It should be noted that these points are the points that were created by the intersection of the reference lines and the centerline with the blade surface.

To map the blade temperature distribution onto the target spots found by the geometric model, it is necessary for this work to match Mackay's. This model includes actual measurements in order to use the analysis functions of the CADAM system, while the geometry associated with Mackay's gas path analysis is on a non-dimensional basis. First, an equation for the track of the pyrometer across the blade is determined in x, y, and z coordinates. Then, the equation is converted to percent height (H) and percent chord (X/C). Percent height and percent chord are the non-dimensional coordinates used by Mackay to describe the blade geometry [13]. The endpoints of the centerline

of the focusing envelope determine the equation for the track of the pyrometer. For the pyrometer installation in the JT15D-1, this equation is:

$$ZLOC = 0.4670(XLOC) + 0.7572 \tag{5.1}$$

To convert this equation to percent height as a function of percent chord, the blade height, chord length, and stagger angle are required. For the present engine, the blade height is equal to 1.175 inches from the cross section at six percent blade height to the cross section at ninety-two percent blade height. The chord length and stagger angle at the portion of the blade where the pyrometer traces are determined by using a linear interpolation. The interpolated blade chord length is 0.7242 inches and the interpolated stagger angle is 45 degrees. This information determines the following equation for the pyrometer path:

$$H = 0.1821(X/C) + 0.6147 \tag{5.2}$$

This equation represents the path traced across the blades by the pyrometer, as shown in Figure 15. Equation 5.2 is input into Mackay's code to determine the temperatures at various points of the target spots for a specific engine speed.

Figure 16 shows the predicted blade temperature distribution along the path of the pyrometer for N2 engine speeds of eighty-five and ninety-five percent. The temperature distribution is then mapped onto the target spots. Table 2 summarizes the incremental areas and temperatures across the target spots for engine speeds of eighty-five and ninety-five percent.

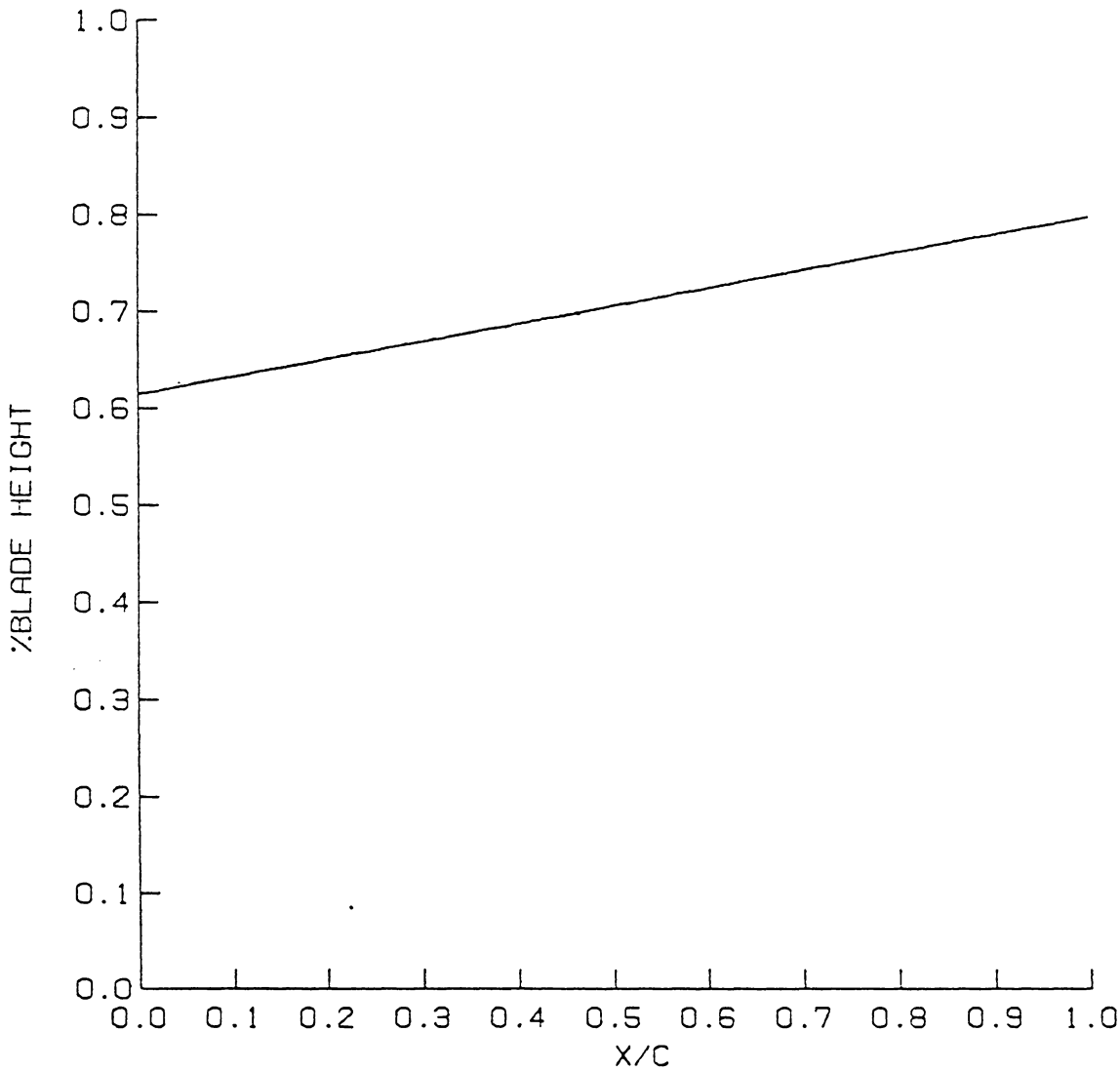

Figure 15. Pyrometer Sight Path Centerline (X/C vs. H)

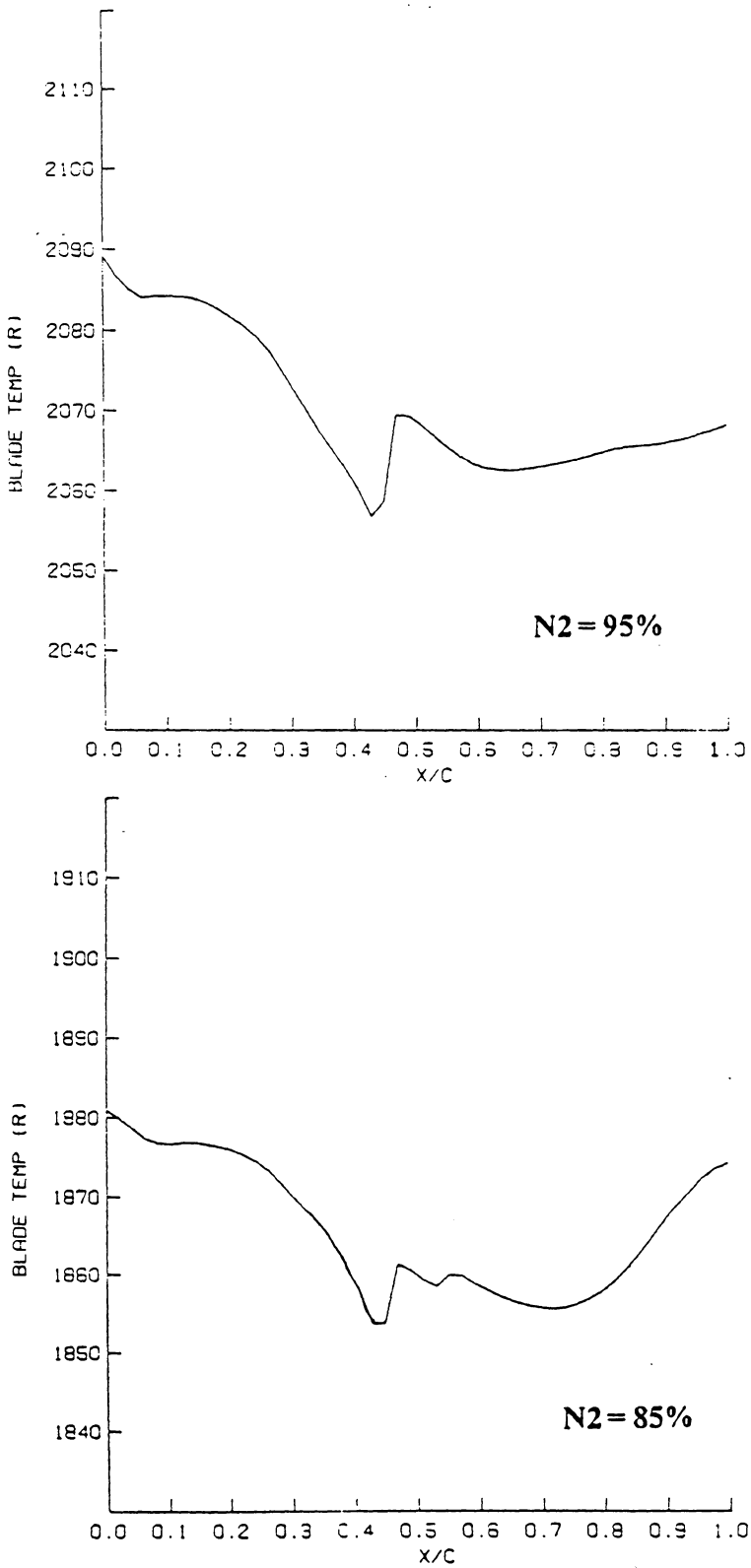

Figure 16. Predicted Temperature Distributions (from Ref. 13)

Table 2. Incremental Areas and Temperature Distribution of Target Spots

Target Spot One			
Area		N2 = 85%	N2 = 95%
No.	Sq. inches	T (R)	T (R)
1	0.0036	1858.7	2063.3
2	0.0025	1858.0	2062.7
3	0.0036	1857.0	2062.6
Target Spot Two			
Area		N2 = 85%	N2 = 95%
No.	Sq. inches	T (R)	T (R)
1	0.0037	1855.7	2063.0
2	0.0026	1855.6	2063.1
3	0.0036	1855.7	2063.2
Target Spot Three			
Area		N2 = 85%	N2 = 95%
No.	Sq. inches	T (R)	T (R)
1	0.0039	1856.9	2064.2
2	0.0024	1857.7	2064.6
3	0.0038	1858.9	2065.1
Target Spot Four			
Area		N2 = 85%	N2 = 95%
No.	Sq. inches	T (R)	T (R)
1	0.0040	1862.8	2065.5
2	0.0026	1865.2	2065.7
3	0.0037	1867.6	2065.9
Target Spot Five			
Area		N2 = 85%	N2 = 95%
No.	Sq. inches	T (R)	T (R)
1	0.0041	1872.5	2067.1
2	0.0025	1873.3	2067.5
3	0.0038	1873.6	2067.7

5.3 Application of Responsivity and Transmission Curves

Once the incremental areas and temperatures are known, the next step is to apply the responsivity curve of the detector being used and the transmission curve of the optical system. Both the responsivity curve and transmission curve are a function of wavelength and can be obtained from a pyrometer manufacturer. Figure 17 shows curves for a typical silicon (Si) detector and a typical indium gallium arsenide (In Ga As) detector. A comparison of the two curves is shown in Figure 18. It can be readily seen that the indium gallium arsenide detector has a higher response energy level than the silicon detector, and also operates over a wider range of wavelength. Therefore, it should be anticipated that the signal obtained from the In Ga As detector will be much larger than for the Si detector.

The transmission curve of the present optical system cannot be presented due to a proprietary restriction. However, in order to predict an accurate signal, the pertinent information associated with the transmission curve is included in the model. The transmission curve describes the percentage of radiation which is transmitted to the detector.

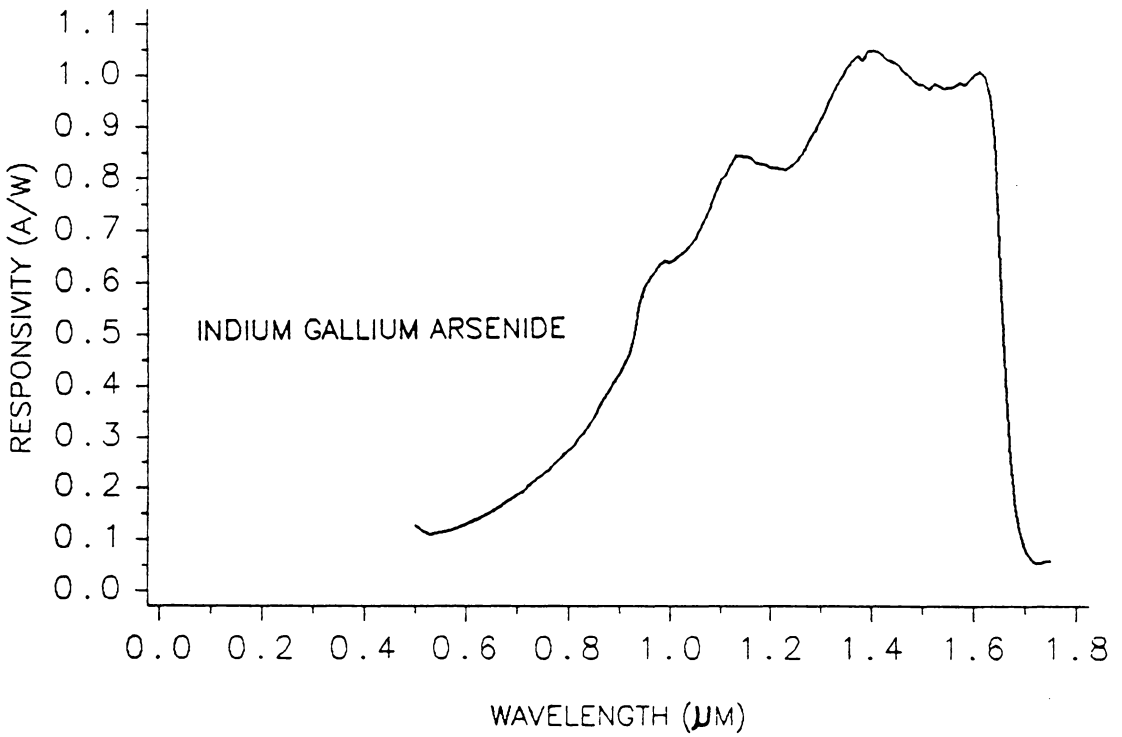

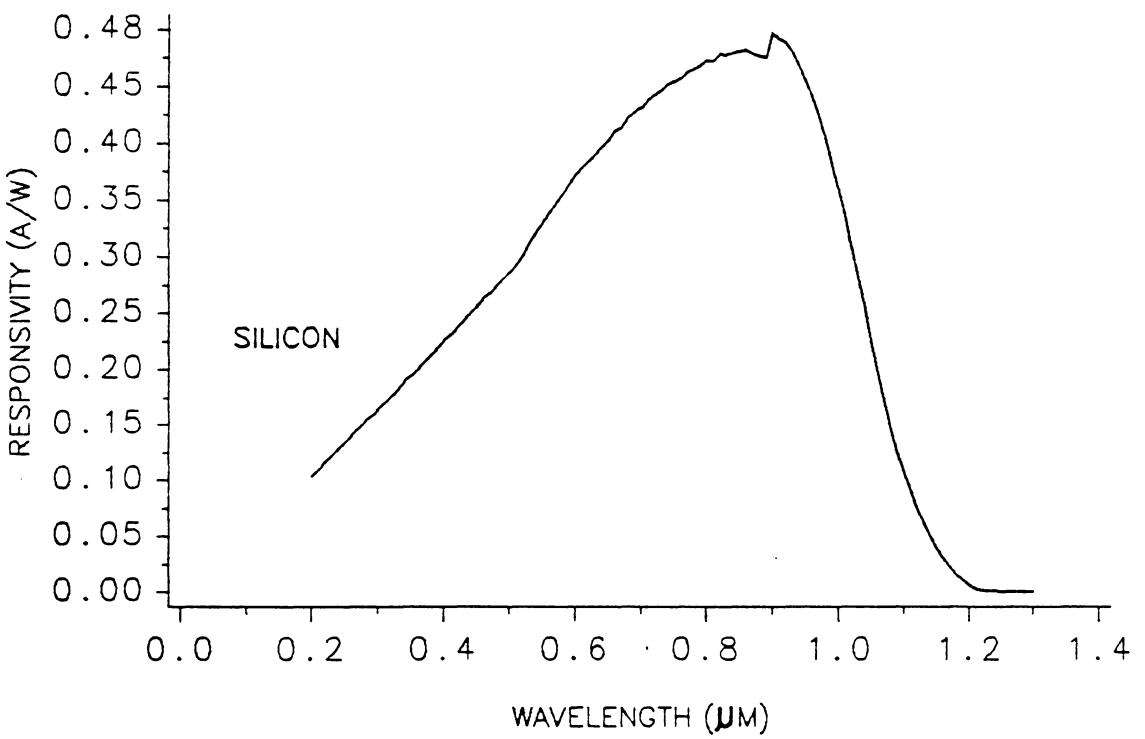

Figure 17. Responsivity Curves

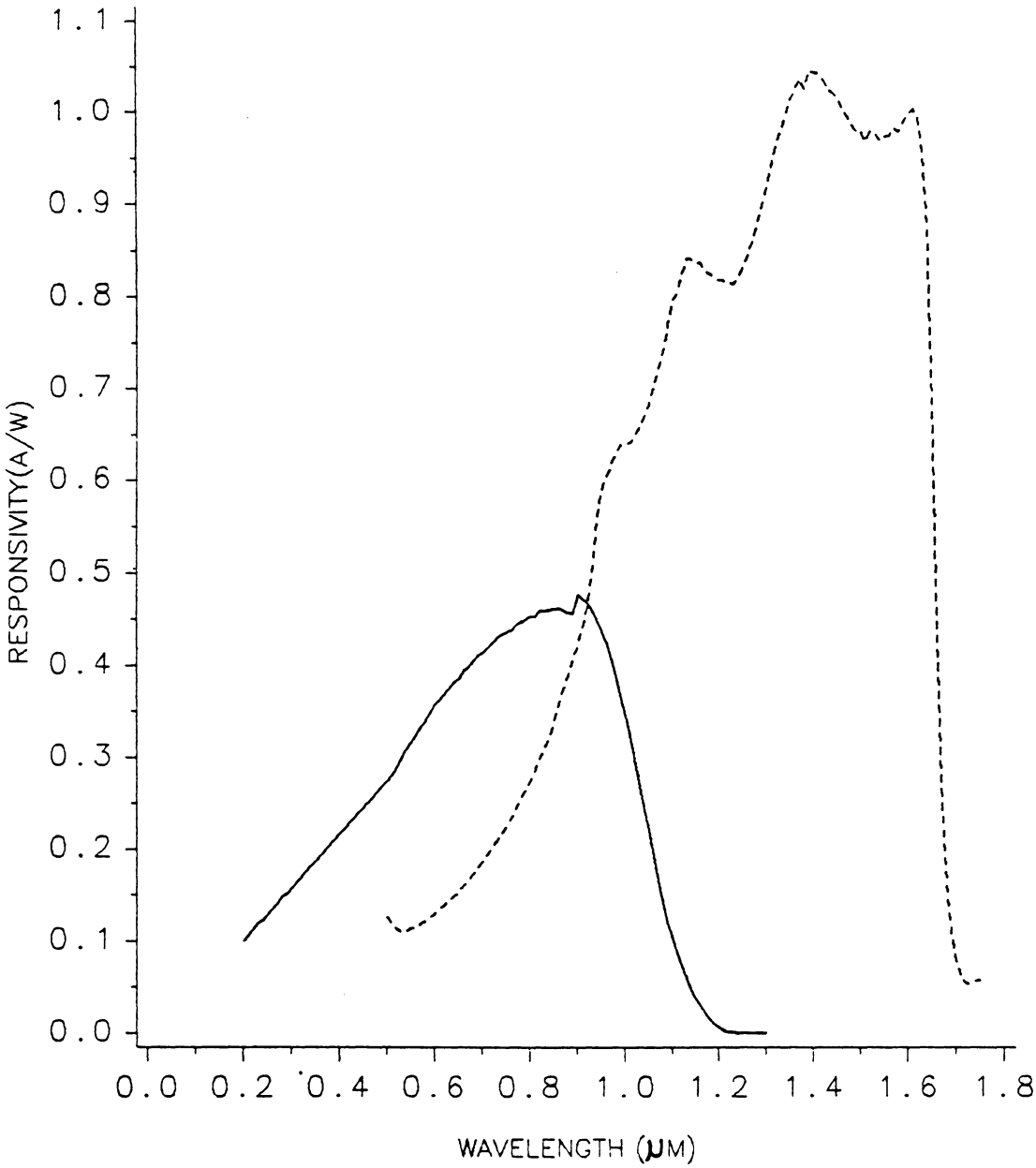

DETECTOR RESPONSIVITY(A/W) ——— SILICON
- - - - - - - - IN GA AS

Figure 18. Comparison of Responsivity Curves

5.4 Photocurrent Prediction

The previous information can be used to predict the output photocurrent of the pyrometer detector. The following equation determines the output photocurrent of a detector and is valid only at the focal plane [20]:

$$I(T) = \Omega_f \int_{A_f} \int_\lambda R(\lambda) L(\lambda, T) \eta(\lambda) d\lambda dA_f \tag{5.3}$$

Where Ω_f is the solid angle of the focused target spot, A_f is the area of the focused target spot, λ is wavelength, R is the detector responsivity, L is blackbody radiation, T is the target spot temperature, and η is the transmission factor of the optical system. The subscript f denotes the parameters associated with the focused target spot. After integrating equation 5.3 over the area of the focused target spot, the resulting equation is :

$$I(T) = \Omega_f A_f \int_\lambda R(\lambda) L(\lambda, T) \eta(\lambda) d\lambda \tag{5.4}$$

The solid angle of the focused target spot, Ω_f, is found by dividing the area of lens by the square of the focal distance of the lens.

The actual target spots are not located at the focal plane, so these spots are slightly "out of focus". The solid angles for the actual target spots are not as easy to determine because not all of the radiation from "out of focus" spots reaches the detector. It therefore becomes difficult to predict the photocurrent from the actual target spots. An elaborate ray tracing algorithm is required to determine the radiation received by the detector from an "out of focus" target spot. However, for a given system, the optical invariant (ΩA) remains approximately constant. This implies that no energy is gained or lost from the

focusing envelope of the pyrometer. Since $\Omega_f A_f$ is known and constant, the solid angle of the actual target spots may be found from the following relation :

$$\Omega_i = \frac{\Omega_f A_f}{A_i} \tag{5.5}$$

Where Ω_i is the solid angle of target spot i and A_i is the area of target spot i. So to determine the photocurrent of the actual target spots the following equation is used :

$$I_i(T) = \frac{\Omega_f A_f}{A_i} \int_{A_i} \int_\lambda R(\lambda) L(\lambda, T) \eta(\lambda) d\lambda dA_i \tag{5.6}$$

Each target spot i is divided into three incremental areas (j). Dividing the target spot into smaller areas produces a more accurate representation of the target spot temperature than assuming the spot is at a single temperature. The current associated with each target spot i is obtained by summing the energy levels of each incremental area j of target spot i. The energy level consists of a given area multiplied by the integral of the responsivity curve, transmission curve, and the blackbody radiation curve over the wavelength range of the detector. So, equation 5.6 becomes:

$$I_i(T) = \Omega_i \sum_{j=1}^{3} A_j \int_\lambda R(\lambda) L(\lambda, T_j) \eta(\lambda) d\lambda \tag{5.7}$$

Where $L(\lambda, T_j)$ is the blackbody radiation from incremental area j at wavelength λ and temperature T_j. $L(\lambda, T_j)$ is found from Planck's law [21].

$$L(\lambda, T) = \frac{C_1}{\lambda^5 (e^{c_2/\lambda T} - 1)} \tag{5.8}$$

C_1 and C_2 are radiation constants and are equal to 3.7415×10^{-4} Wμm^2 and 1.43879×10^4 μmK respectively.

The physical significance of the integral in equation 5.7 is shown on a non-dimensional basis in Figure 19. The intersected area of the two curves represents the output energy of the detector per unit area.

The optical factor, $\eta(\lambda)$, included in the integral decreases the output energy of the detector by a certain percentage. The reason is that no optical system has an optical factor equal to one. It should be noted that due to a proprietary restriction, the values used for the optical factor, $\eta(\lambda)$, were not absolute values. The values were normalized by dividing each value by the maximum value of the optical transmission curve. The result is a predicted signal which has correct dynamics, but has an absolute value which is in error by a factor of a constant.

The integral in equation 5.7 is numerically evaluated using Simpson's rule [22]. The result obtained after finding the current output associated with each target spot i is a predicted signal versus percent chord. This predicted signal is shown in Figure 20 for a Si detector at an engine speed equal to ninety-five percent. The upper part of Figure 20 shows that in the JT15D-1 application the pyrometer traces from sixty-one percent chord to one-hundred percent chord. One-hundred percent chord is at the trailing edge of the blade.

To convert the signal to a time base, percent chord must be converted to seconds. This is done by applying the following two equations:

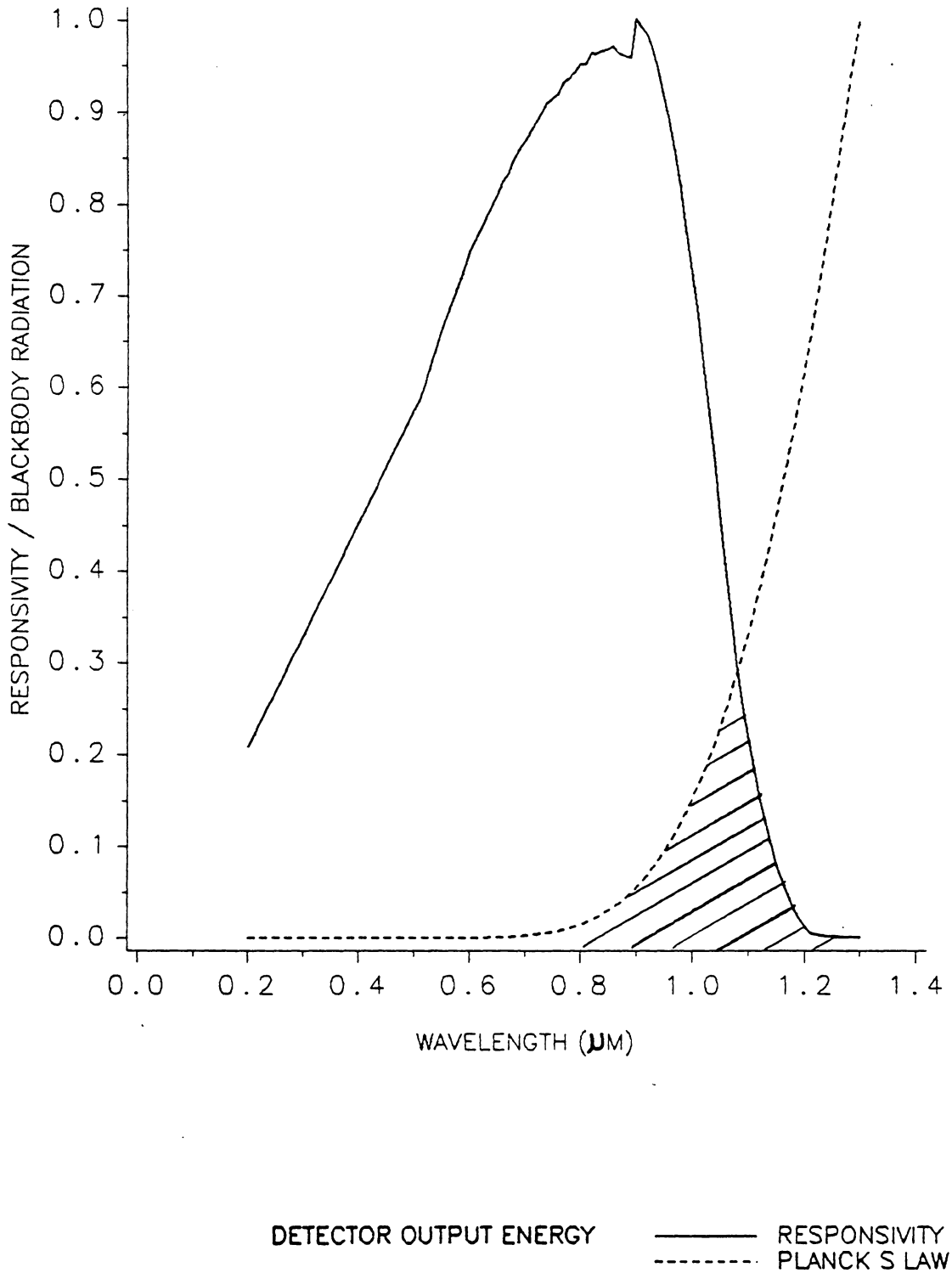

Figure 19. Intersection of Responsivity Curve and Blackbody Radiation Curve

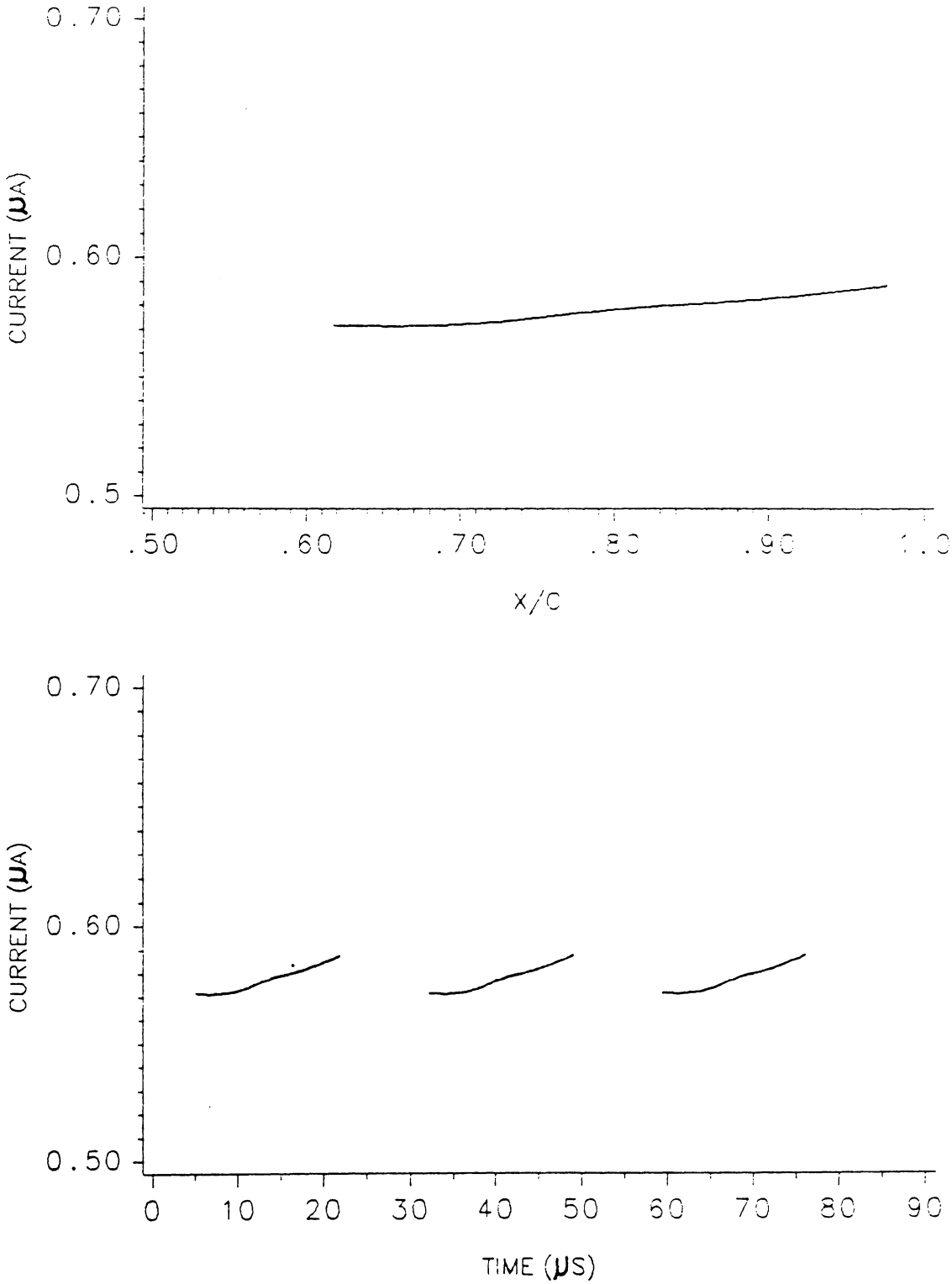

Figure 20. Predicted Pyrometer Signal : Si Detector, N2 = 95%

$$TIME = \left(\frac{N2(\#blades)}{60}\right)^{-1} \tag{5.9}$$

$$BPT = \left(\frac{(X/C - CMIN)}{CMAX - CMIN}\right)TIME \tag{5.10}$$

N2 is the engine speed in revolutions per minute and TIME is in seconds. CMIN and CMAX are the minimum and maximum percent chord values of the viewable blade width. So, BPT is the blade passing time between the center points of the target spots. The resultant output signal versus time for a Si detector at ninety-five percent speed is shown in the lower part Figure 20, which shows the repetitive nature of the pyrometer signal. Since an analog signal is continuous, an actual recorded signal would appear as a continuous waveform. Only the data portion of the signal predicted by the model is shown in the figure.

5.5 Results

5.5.1 Analytical

The strength of an output signal of a pyrometer is a function of the spot size, target temperature, and type of detector being used. Large spot sizes and higher temperatures imply a stronger signal. The spot size associated with the JT15D-1 pyrometer work is very small in order to do profile work. Here, it is desired to obtain an accurate temperature distribution of the blade instead of an average temperature of the turbine disk.

The energy associated with the target spot of a pyrometer is the average of the temperature distribution over the area of the target spot. So, the smaller the spot size, the more accurate is the representation of the temperature distribution. Physically, this can be understood by knowing that the true temperature distribution corresponds to a point or a zero spot size. Since the blade temperatures associated with the JT15D-1 are low and a small spot size is being used, the proper choice of detector is very important.

Part of a pyrometer research program is to evaluate the proper type of detector to use. Even with the use of fiber optics, a pyrometer detector is located in a harsh environment which is subject to changes in ambient temperature. As mentioned before, the Si detector is the most popular choice of detector because it is less sensitive to thermal drift. However, for engines with low blade temperatures, the signal from the Si detector is weak and very susceptible to noise. So, to obtain a higher output current, an In Ga As detector can be used. This detector is sensitive to changes in the surrounding temperature, so a means must be employed to keep the detector at an equilibrium temperature. One method is the use of a heater, but these can be very bulky and do not lend themselves to flight applications. Heaters can be used in a test cell environment for diagnostic applications.

The present work involves comparing the difference in signals between a Si detector and an In Ga As detector. These signals are compared at the JT15D-1 design speed, ninety-five percent, and at an off-design speed of eighty-five percent. The results from the geometric analysis showed that the pyrometer can only view from sixty-one percent chord to one hundred percent chord (trailing edge). Examination of Table 1 shows that the pyrometer detects a temperature change of eighteen degrees C at eighty-five percent and a temperature change of five degrees C at ninety-five percent. So, the recorded

output signal of the detector will vary more from peak to peak for the eighty-five percent case. The predicted output signal for a Si detector with an engine speed of ninety-five percent was shown in Figure 20. Figure 21 shows the predicted output signal for an In Ga As detector at an engine speed of ninety-five percent versus percent blade chord and time. Figures 22 and 23 show predicted signals for a Si and an In Ga As detector at an off design speed of eighty-five percent.

When the two predicted signals are compared at eighty-five percent, it can be seen that the signal from the Si detector is at a much lower level than the In Ga As detector. This is represented in Figure 24. Even if the gain on the amplifier of the Si detector was turned up so the two detectors had signals at the same voltage level, this would not solve the problem. The reason is because the noise on the signal produced by the Si detector would also be amplified. Therefore, in order to obtain a cleaner signal in the present application, the In Ga As detector should be used at eighty-five percent engine speed. It can also be postulated that at lower engine speeds, the In Ga As detector would be better than the Si detector because the temperatures would be lower. Figure 25 shows that even at design speed, the Si detector gives a small signal. All of these results imply that the In Ga As detector should be used with a heater to take pyrometer data in the present application.

The final analytical result presented is the comparison between a pyrometer signal obtained from a cooled turbine blade and the signal obtained from an uncooled blade. The JT15D-1 has uncooled turbine blades. However, most modern engines have cooling associated with at least the first stage turbine rotor. The model is therefore applied to a cooled blade to show the characteristics of a pyrometer signal obtained from a more modern turbine.

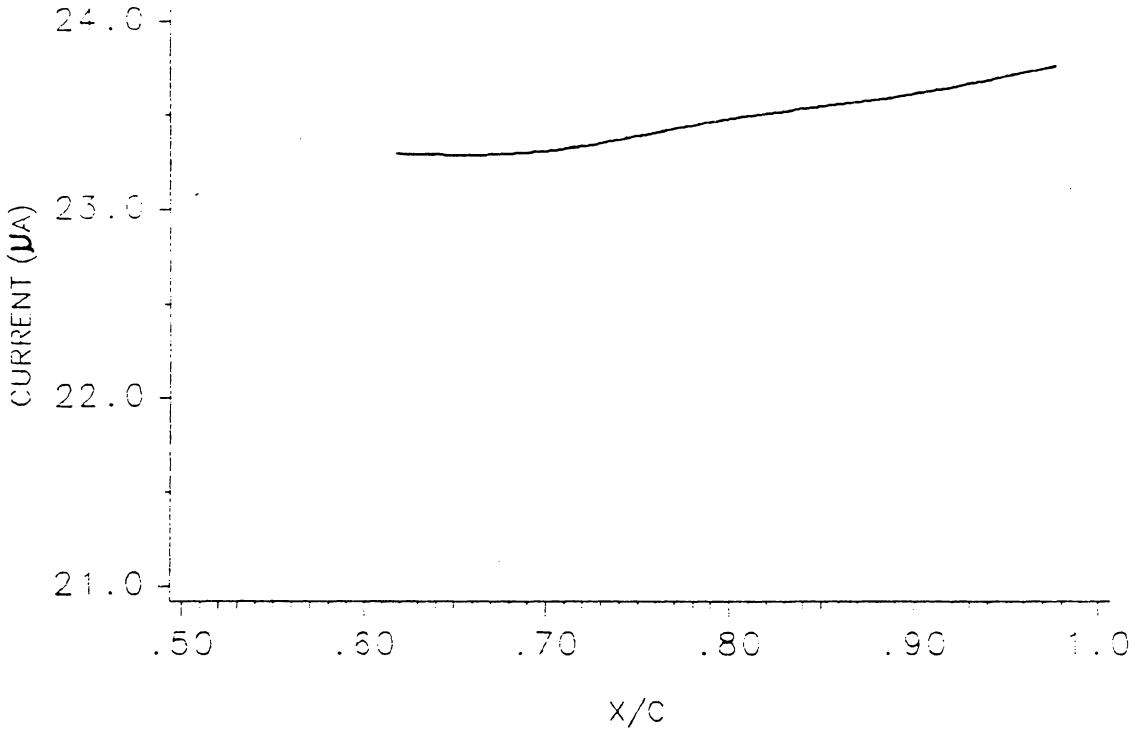

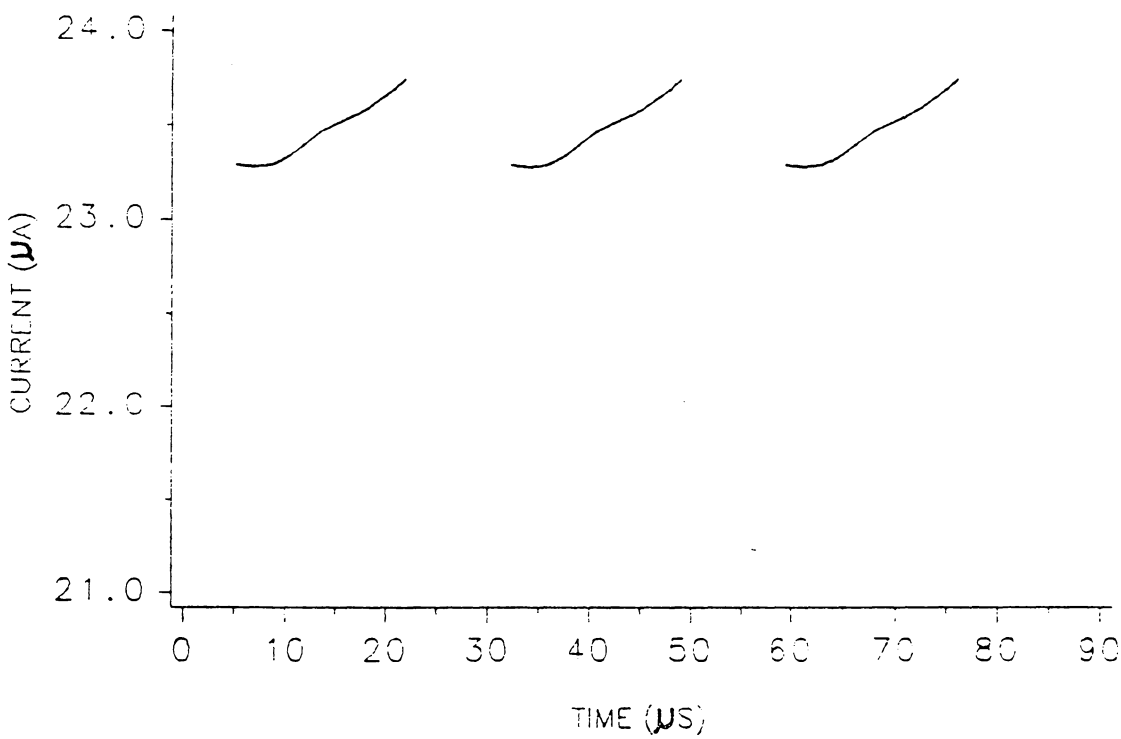

Figure 21. Predicted Pyrometer Signal : In Ga As Detector, N2 = 95%

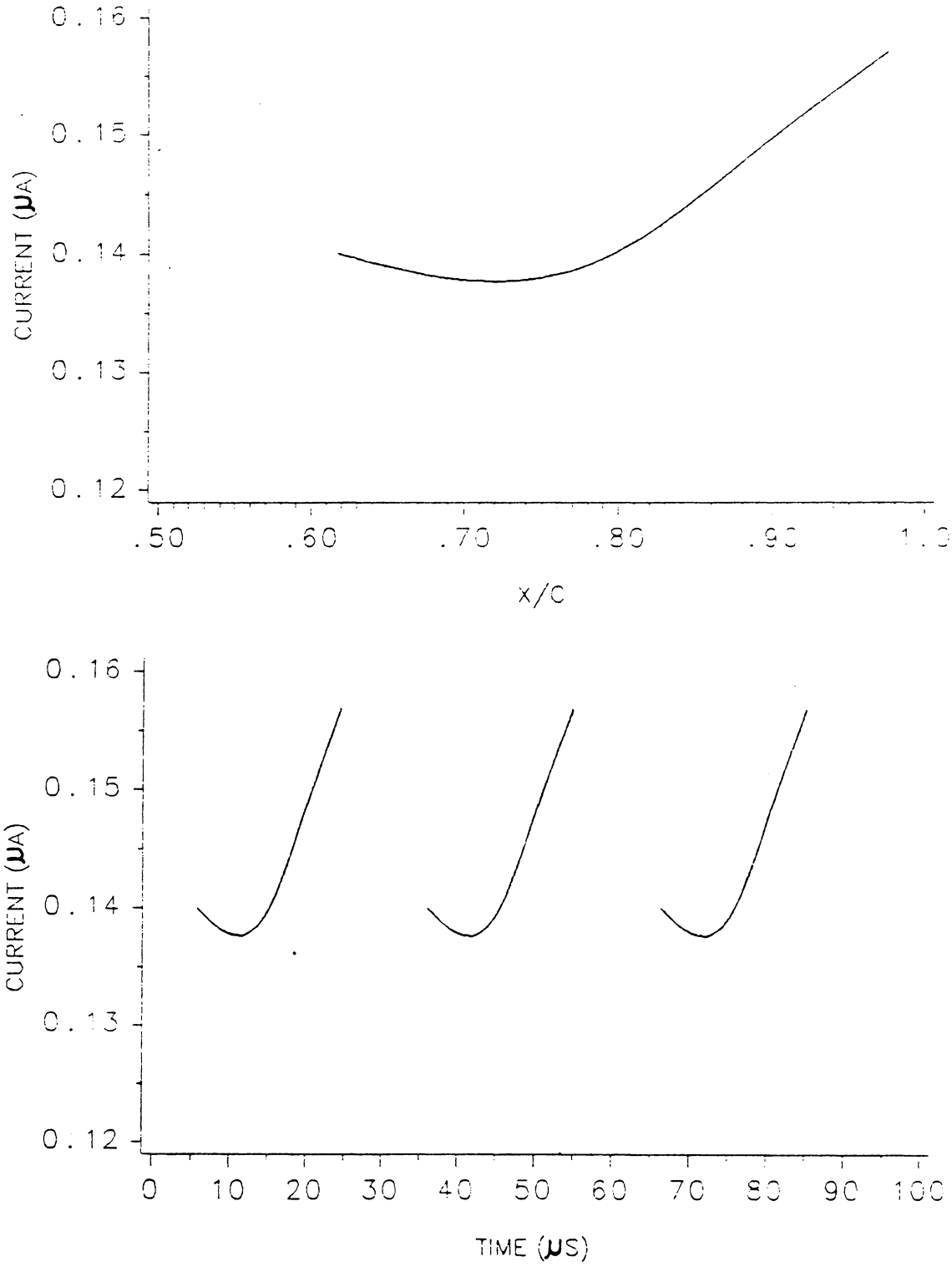

Figure 22. Predicted Pyrometer Signal : Si Detector, N2 = 85%

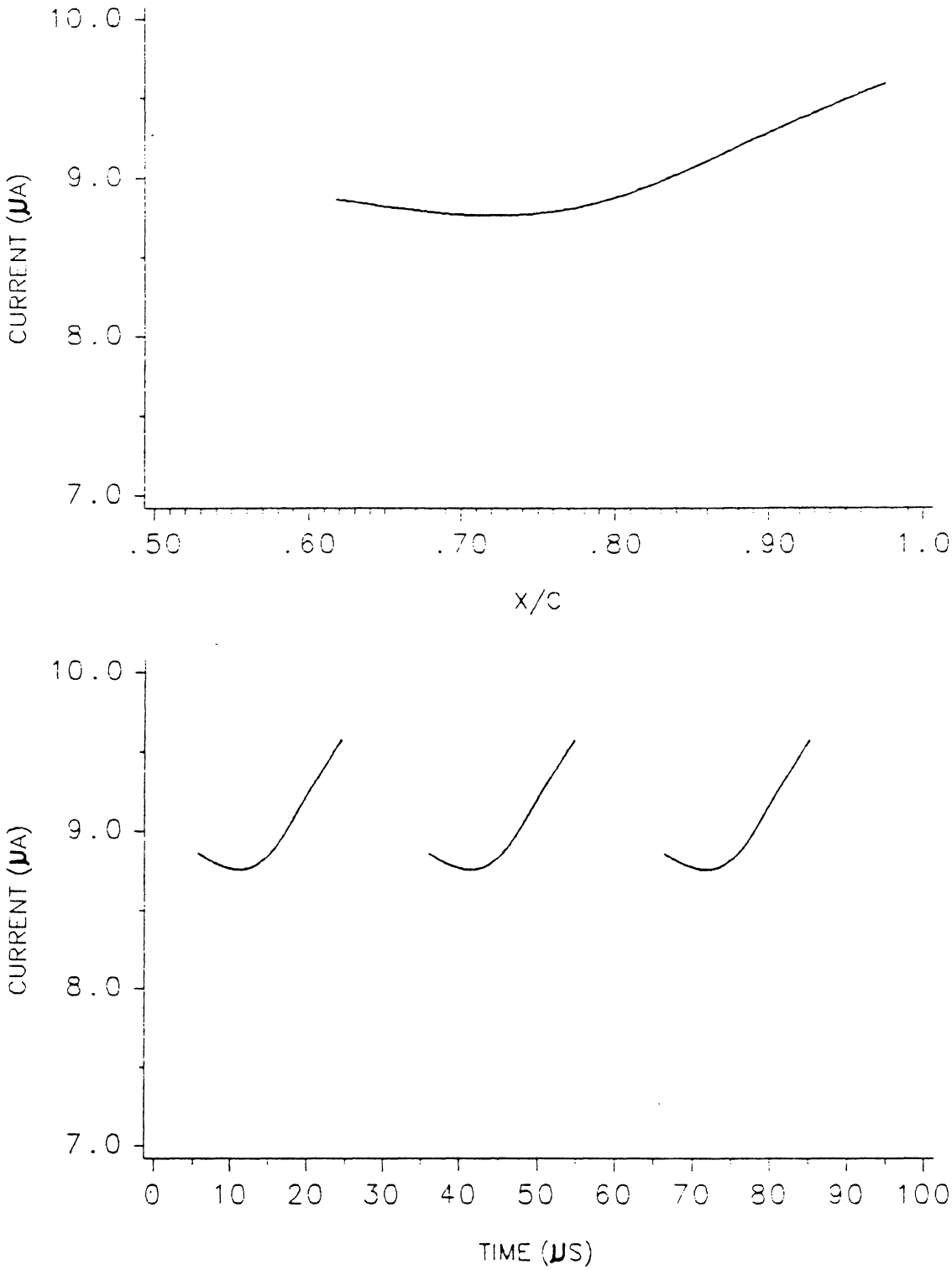

Figure 23. Predicted Pyrometer Signal : In Ga As Detector, N2 = 85%

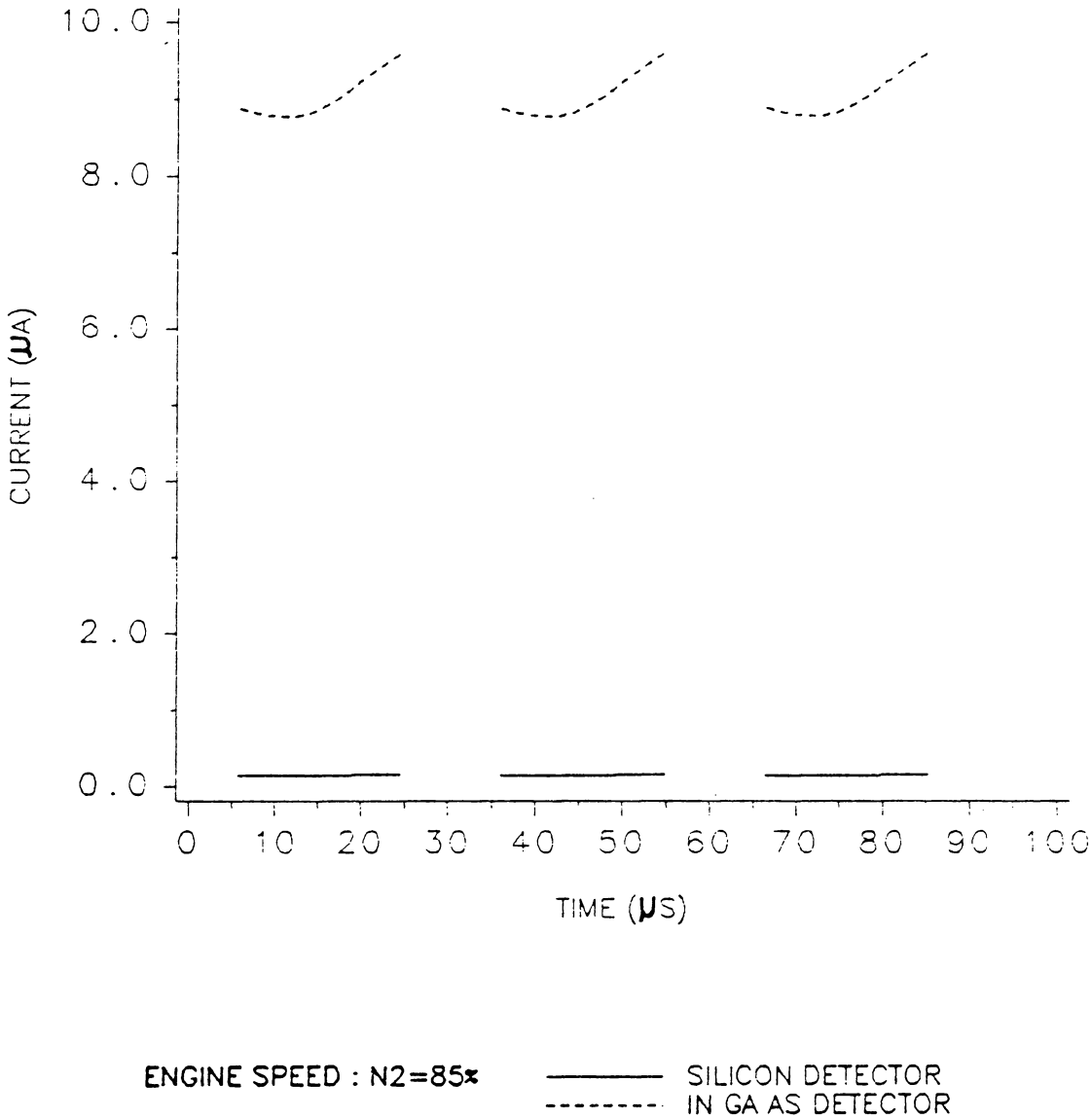

Figure 24. Comparison between Predicted Detector Signal Levels, N2 = 85%

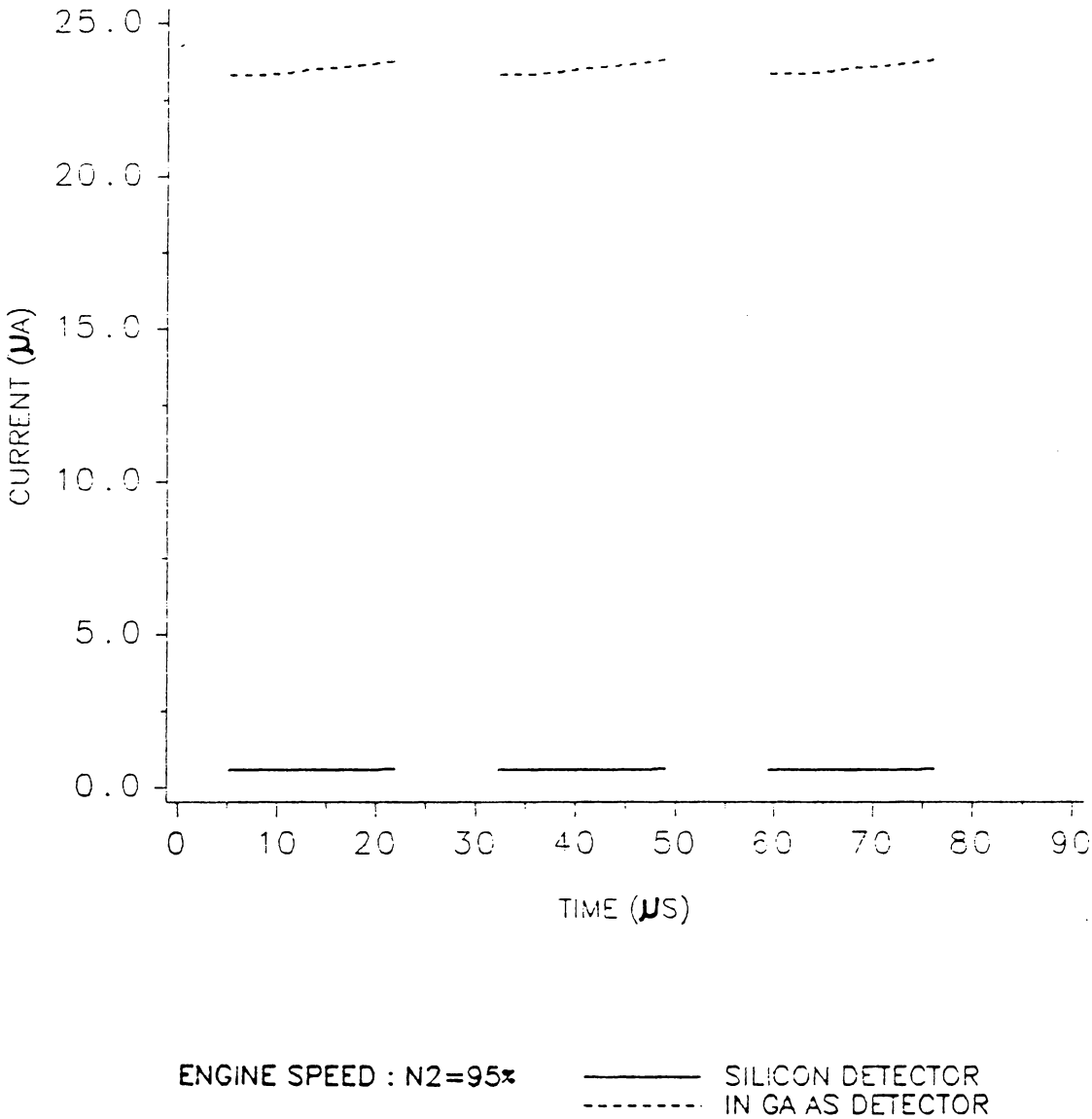

Figure 25. Comparison between Predicted Detector Signal Levels, N2 = 95%

Reference 12 contains a thermal map of a cooled turbine blade from an industrial gas turbine. This blade has temperatures in the same range as the JT15D-1 operating at an engine speed of eighty-five percent. The temperature distribution of the cooled turbine blade was mapped onto the uncooled blade of the JT15D-1 so that a comparison could be made between the signal for the cooled blade and the signal for the uncooled blade. The temperature distributions for the cooled and uncooled blades are given Table 3.

The temperature distribution was mapped from the cooled blade to the uncooled blade by normalizing the geometry of the two blades. The present equation for the line of sight of the pyrometer was then applied in order to obtain a pyrometer signal for a cooled blade. It should be noted that the previous procedure is not exact. The idea is to show the difference between a pyrometer signal for a cooled blade and an uncooled blade of the same geometry and same pyrometer installation. The predicted pyrometer signal for the cooled blade is shown as a function of percent blade chord and as a function of time in Figure 26. Figure 27 shows a comparison of the two predicted signals as a function of percent blade chord. It can be seen that the two signals are very different, due to the different temperature distributions.

All turbine blades, cooled and uncooled, have unique temperature gradients. Figure 27 clearly shows that the shape of a pyrometer signal is strongly affected by the temperature gradient detected by the instrument. The knowledge of the exact path which the pyrometer sight area traces across a blade is very important. With this information, the installation parameters of the pyrometer can be varied so as to obtain the best signal for a given application. The model allows the freedom to vary the installation parameters and then to compare the difference between signals.

Table 3. Temperature Distributions for Cooled and Uncooled Blade

Target Spot One			
Area		Uncooled Blade	Cooled Blade
No.	Sq. inches	T (R)	T (R)
1	0.0036	1858.7	1908.6
2	0.0025	1858.0	1923.0
3	0.0036	1857.0	1926.6
Target Spot Two			
Area		Uncooled Blade	Cooled Blade
No.	Sq. inches	T (R)	T (R)
1	0.0037	1855.7	1923.0
2	0.0026	1855.6	1905.0
3	0.0036	1855.7	1901.4
Target Spot Three			
Area		Uncooled Blade	Cooled Blade
No.	Sq. inches	T (R)	T (R)
1	0.0039	1856.9	1896.0
2	0.0024	1857.7	1890.6
3	0.0038	1858.9	1888.8
Target Spot Four			
Area		Uncooled Blade	Cooled Blade
No.	Sq. inches	T (R)	T (R)
1	0.0040	1862.8	1887.0
2	0.0026	1865.2	1869.0
3	0.0037	1867.6	1842.0
Target Spot Five			
Area		Uncooled Blade	Cooled Blade
No.	Sq. inches	T (R)	T (R)
1	0.0041	1872.5	1824.0
2	0.0025	1873.3	1820.4
3	0.0038	1873.6	1818.6

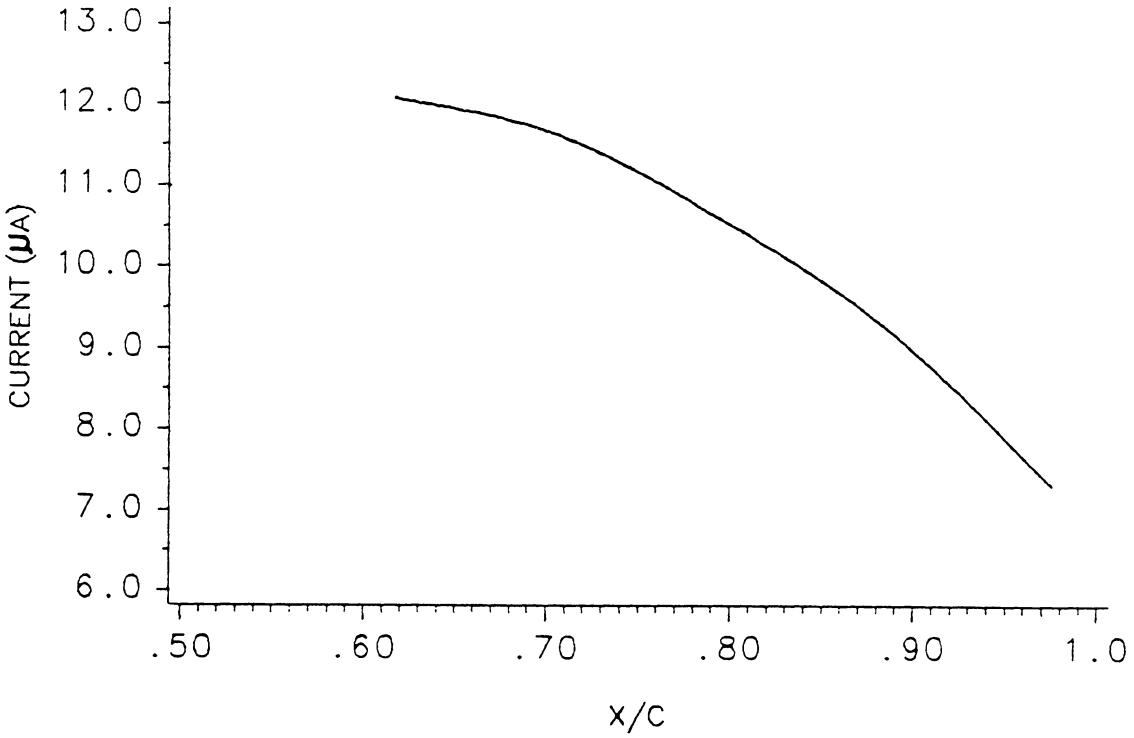

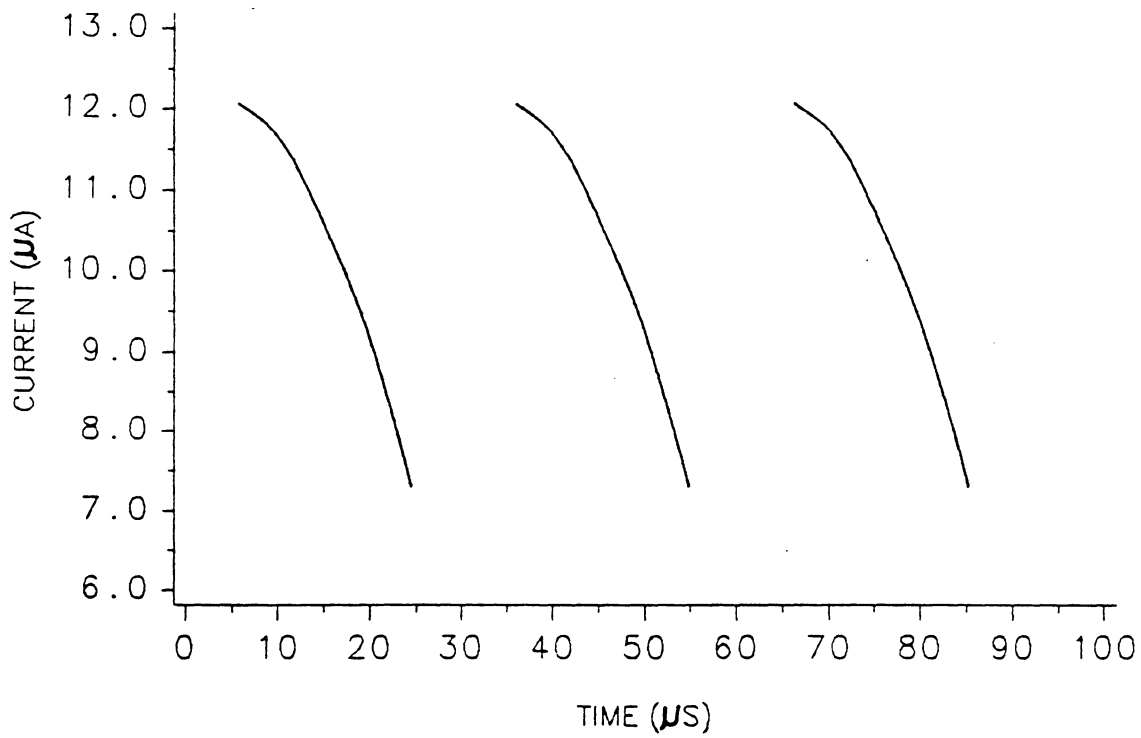

Figure 26. Predicted Signal : Cooled Blade, In Ga As Detector, N2 = 85%

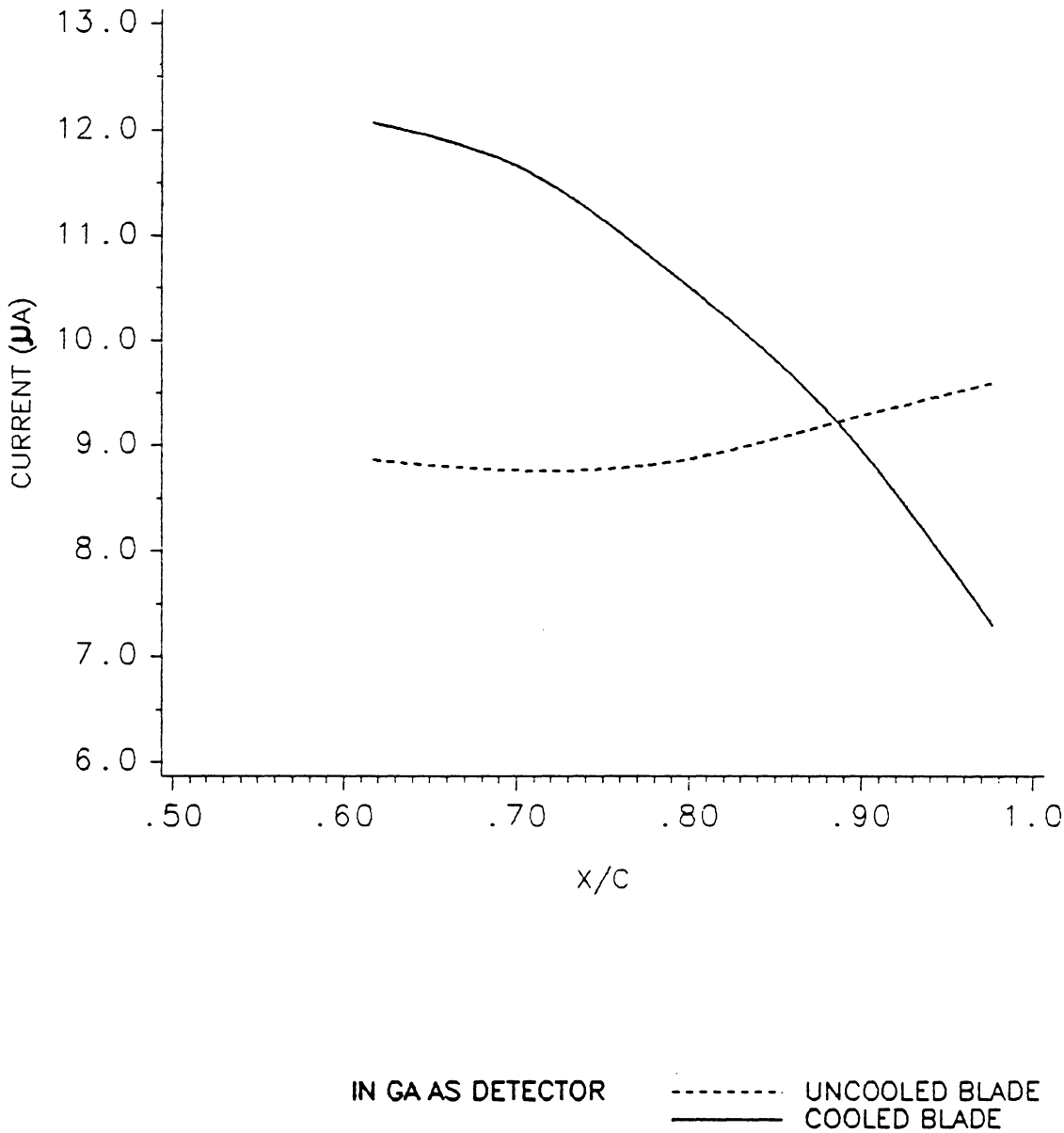

Figure 27. Comparison of Signals for Cooled Blade and Uncooled Blade

5.5.2 Experimental Measurements

The data acquisition system for a pyrometer is very important. The system must be fast enough to digitize and accurately capture the information transduced by the detector. The detector must also have a response time fast enough to detect the radiation from each individual target spot. The response time of the detector is matched to the spatial resolution of the pyrometer. The response time or electronic bandwidth of the detector is found by the following equation [2]:

$$f_s = f_b(w/d) \tag{5.11}$$

Where w/d is the spatial resolution of the pyrometer and represents the number of target spots per blade.

For the present application f_s should be at least five times the blade passing frequency since there are five target spots per blade. At design speed, the blade frequency of the JT15D-1 is approximately 37 kHz. So the detector should have an electronic bandwidth of at least 185 kHz. The bandwidth of the detectors being used are in an acceptable range, having electronic bandwidths greater than 200 kHz. As a general rule, to prevent serious aliasing, the data acquisition system should have a bandwidth of at least twice that of the detector. The pyrometer data taken on the JT15D-1 is recorded on a Lecroy high speed digitizer and then sent to a computer. The Lecroy has an adequate sample rate of one microsecond.

The first pyrometer data taken on the JT15D-1 was with a single channel pyrometer incorporating a Si detector. The recorded pyrometer traces were at a low level, almost flat,

and had a low signal-to-noise ratio. It was then decided to implement an In Ga As detector with a heater to keep the detector at an equilibrium temperature. The pyrometer signal recorded from the In Ga As detector was at a higher level and a distinction could be made between individual blades. There was still some noise associated with the signal, but less than with the Si detector. The next phase of the research program was to take pyrometer data with a two channel pyrometer. One channel used a Si detector and the other an In Ga As detector. The amplifier gain was increased for the Si detector so that the voltage levels of the two signals would be at the approximately the same level. A comparison between the two signals at an engine speed of eighty-five percent is shown in Figure 28. As expected, the signal associated with the Si detector contains a large amount of noise. The signal from the In Ga As detector has some noise, but a distinction can be made between individual blades. Both the experimental results and the results from the model imply that the In Ga As detector should be used.

Due to the proprietary nature of the data, a direct comparison cannot be made between the experimental data and the model. The first reason is that the modeled signal uses an optical transmission curve which has been normalized. Secondly, the model predicts the output photocurrent of the detector and the recorded experimental data is the voltage output of the amplifier which has passed through a filter. Since the amplifier has a linear gain, a comparison can be made on a normalized basis between the modeled photocurrent and the recorded voltage. Also, since emissivity is approximately constant for oxidized steel, a comparison between the actual data and the model is valid on a normalized basis because the emissivity factor is eliminated [23]. Each data point of the recorded signal is divided by the maximum value of the recorded signal. The result is a signal that has a range in peak to peak amplitude of zero to one. The same idea is applied to the modeled signal. When the recorded signal and the modeled signal are com-

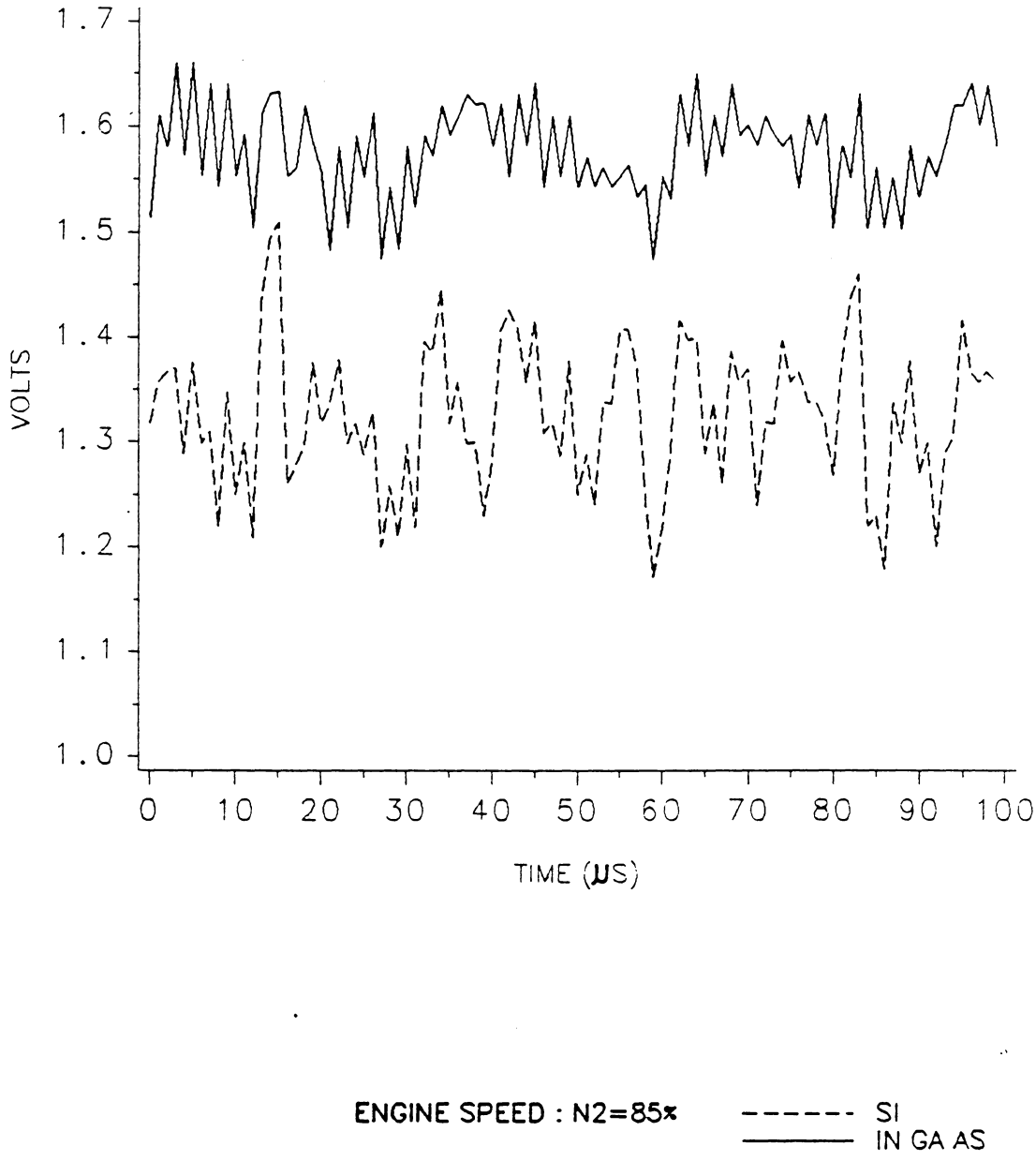

Figure 28. Experimental Pyrometer Data

pared on a normalized basis, a comparison can be made between the dynamics of the two signals. Figure 29 shows a comparison of the model results and the data for an In Ga As detector at an engine speed of eighty-five percent.

The experimental data represented in Figure 29 is different from the data in Figure 28. The detector unit of the pyrometer system, which was used to take the data shown in Figure 29, was placed in the control room instead of in the test cell. A new fiber optic design was also implemented with this system. Because of a more favorable detector environment and a new fiber optic design, the data in Figure 29 contains much less noise than the data in Figure 28. Therefore, due to very little noise, the data in Figure 29 was used in comparison with the modeled signal.

Figure 29 verifies that the dynamics of a pyrometer signal can be predicted by the model. It again should be emphasized that the model cannot predict the lag of the signal between the blades. The model only predicts the portion of the signal which is due to the focusing geometry of the pyrometer and the temperature distribution across the blade. The signal lag shown in the experimental data is due to a filter [24]. If a filter was not used, the dynamics of the modeled signal and the experimental data should compare more closely. However, due to the response time of the detector being used, a filter is applied to prevent the possibility of aliasing.

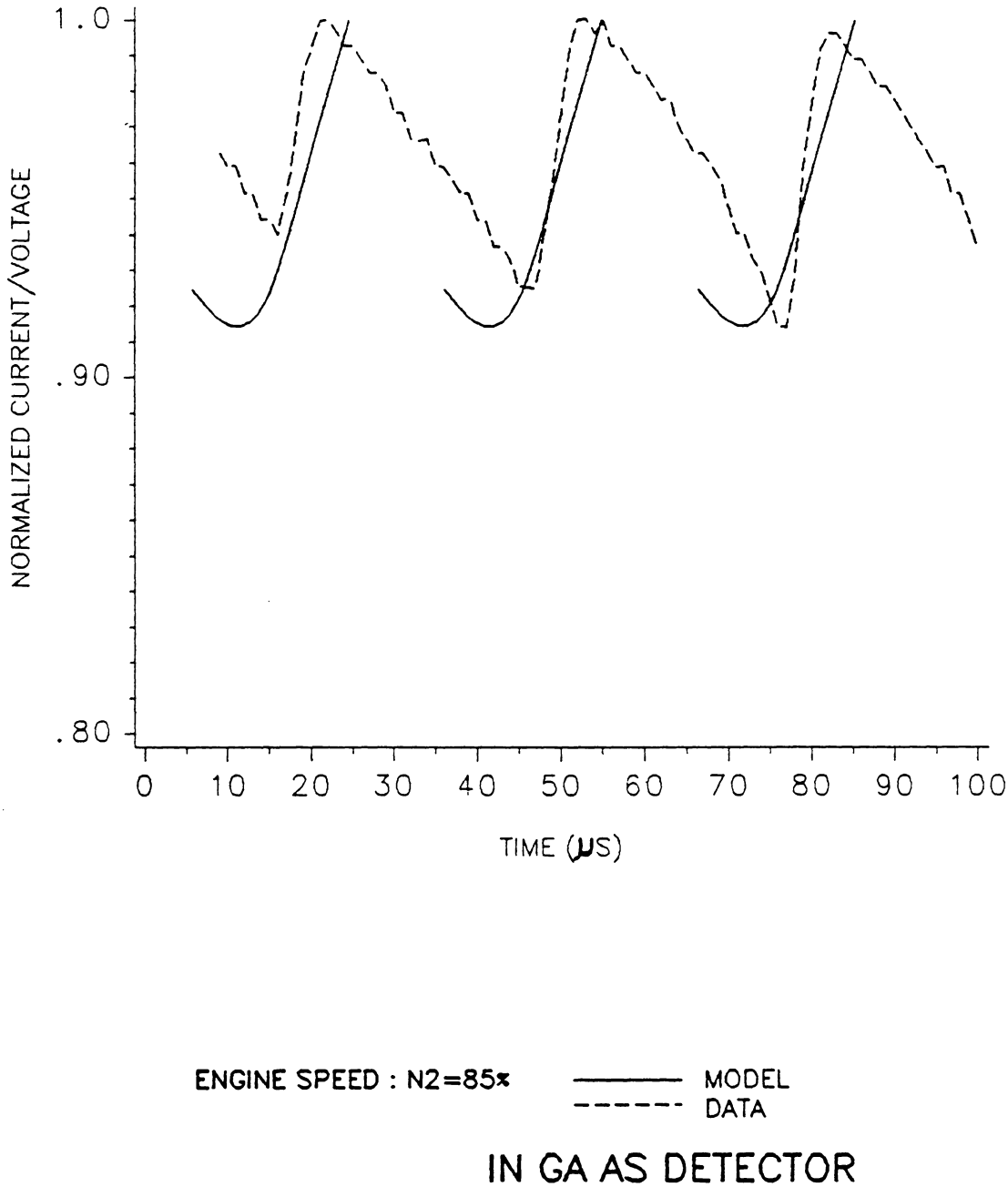

Figure 29. Comparison of Model and Data

5.6 Summary

The model has been shown to be a very useful tool. The model may be applied at the initial design phases of a pyrometer program to determine which set of installation parameters, focusing parameters, and type of detector is the best for a particular application. The model may also be applied to compare the predicted results with the experimental data. This comparison will reveal information concerning the dynamics of the signal. It will also help with the elimination of noise sources and aid with the determination of proper signal processing techniques.

Chapter 6

Conclusions

The model described in this thesis showed a three-dimensional representation of the blade geometry, trace of the pyrometer across the blades, and the intercepted target spots. The model also predicted the output photocurrent of a particular detector for a given temperature distribution.

The path the pyrometer traces across the blades and the intercepted target spots was found from the geometric model. The geometric model can be applied to any pyrometer installation in an axial flow turbine. The model allows different pyrometer installations to be evaluated before implementing a pyrometer in a jet engine.

The dynamics of a pyrometer signal were determined by using the target spot areas and the trace of the pyrometer across the blades along with an estimated blade temperature distribution, detector responsivity curve, and an optical transmission curve. The dynamics of the modeled signal correlated well with the experimental data taken during the pyrometer research program. Knowledge concerning the dynamics of a pyrometer signal

can be used to eliminate noise sources and to determine appropriate signal processing techniques.

Finally, this work was also used to determine the proper bandwidth of the detector required for a given spot size and engine speed. Once the detector bandwidth was determined, the proper choice of data acquisition system was implemented.

Chapter 7

Future Recommendations

Several topics are recommended for future study in the area of pyrometer system analysis. The first is the creation of an analytic radiation model which includes reflected radiation, combustion particles, and varying emissivity. This radiation model should also take into account the complicated geometries of the view factors. The view factors determine the portion of radiation detected by the pyrometer from various sources. This model could possibly be created with the aid of a CAD system. An accurate radiation model would improve upon the present work; especially if the pressure side of a turbine blade was being viewed. This is because the pressure side of the blade is very susceptible to combustion wall reflections and hot carbon particles.

Another recommended area of research is the design of accurate and reliable methods for calibrating pyrometer systems. A pyrometer which did not have to be removed from the engine for calibration would be beneficial.

Successful methods for maintaining a clean lens are very important. The evaluation of different schemes and designs which supply purge air to the lens of the pyrometer is another recommended topic of study.

Fiber optic technology plays a major role in the creation of a pyrometer system. The research and development of different fiber optic designs will help produce a more reliable and durable pyrometer.

The final area recommended for future study is fast Fourier transform (FFT) analysis of the data. A once per revolution sensor is required in order to apply this method of signal processing. This type of analysis will determine the frequency content of the recorded waveforms. It will also help to determine whether or not an alias has been created on the signal.

References

1. Michalski, L., Personal Communication, Pratt and Whitney Canada, Montreal, Canada, 17 August 1987

2. Kirby, P.J., "Some Considerations Relating to Aero Engine Pyrometry," *AGARD Conference Proceedings No.399, Advanced Instrumentation for Aeroengine Components,* Nov. 1986, pp.17.1-17.14

3. Cook, D.L., "Development of the JT15D-1 Turbofan Engine," *SAE Paper 720352,* pp.1-10

4. Beynon, T.G.R., "Turbine Pyrometry-An Equipment Manufacturer's View," *ASME Paper 81-GT-136,* pp.1-7

5. Beynon, T.G.R., "Radiation thermometry applied to the development and control of gas turbines," *Temperature: Its Measurement and Control in Science and Industry,* v.5 Part I, pp.471-477

6. Douglas, J., "High Speed Turbine Blade Pyrometry in Extreme Environments," "Measurement Methods in Rotating Components of Turbomachinery," *ASME Jt. Fluids Eng. and Gas Turbine Conference New Orleans, LA March 10-13, 1980* pp.335-343

7. Atkinson, W.H., and Strange, R.R., "Pyrometer Temperature Measurements in the Presence of Reflected Radiation," *ASME Paper 76-HT-74,* pp.1-8

8. Hunter, G.B., Allemand, C.D., and Thomas W. E., "Multiwavelength pyrometry: an improved method," *Optical Engineering,* November / December 1985, v.24 No.6, pp.1081-1085

9. Kirby, P.J., Zachary, R.E., and Ruiz, R., "Infrared Thermometry for Control and Monitoring of Industrial Gas Turbines," *ASME paper 86-GT-267,* pp.1-11

10. Koschel, W., Salden, D., and Hoch T., "Turbine Rotor Blade Measurements using Infrared Pyrometry" *AGARD Conference Proceedings No.399, Advanced Instrumentation for Aeroengine Components,* Nov. 1986, pp.18.1-18.16

11. Mossey, P.W., "Experimental Pyrometer for Turbine Blade Temperature Measurement," *SAE Paper 690431,* pp.1-8

12. Schulenberg, T., and Bals, H., "Blade Temperature Measurements of Model V84.2 100MW/60 Hz Gas Turbine," *ASME Paper 87-GT-135,* pp.1-8

13. Mackay, J. D., Personal Communication, Virginia Tech, Blacksburg, Va., 10 September 1986

14. *Cadam Basic Operator Course,* 2nd Edition, SC20-1965-1, IBM, Cadam Inc., 1985

15. *Cadam Interactive User Reference Manual,* v.1, Program Number: 5668-840, IBM, Cadam Inc., 1985

16. *Cadam Interactive User Reference Manual,* v.2, Program Number: 5668-840, IBM, Cadam Inc., 1985

17. *Cadam Geometry Interface Installation Guide,* Program Number: 5668-842, IBM, Cadam Inc., 1985

18. O'Brien, R., Personal Communication, Rosemount Aerospace Division, Eagan, Minnesota, 9 Fegruary 1987

19. Incropera F.P. and Dewitt, D.P., *Fundamentals of Heat Transfer,* John Wiley and Sons Inc., New York, New York, 1981, pp.545-553

20. O'Brien, R., Personal Communication, Rosemount Aerospace Division, Eagan, Minnesota, 15 April 1987

21. Sparrow E.M. and Cess, R.D., *Radiation Heat Transfer,* Hemisphere Publishing Company, London, England, 1978, pp.5-8

22. Atkinson, K., *Elementary Numerical Analysis,* John Wiley and Sons, Inc., New York, New York, 1985, pp.155-165

23. Gray, W.A. and Muller, R., *Engineering Calculations in Radiative Heat Transfer,* Pergamon Press, Oxford, England, 1974, pp.17-19

24. O'Brien, W.F., Personal Communication, Virginia Tech, Blacksburg, Va., 30 July 1987

The vita has been removed from the scanned document